

Elastic-backscatter-lidar-based characterization of the convective boundary layer and investigation of related statistics

S. Pal, A. Behrendt, and V. Wulfmeyer

Institute of Physics and Meteorology (IPM), University of Hohenheim, Garbenstrasse 30, 70599 Stuttgart, Germany

Received: 23 February 2009 – Revised: 5 January 2010 – Accepted: 11 March 2010 – Published: 22 March 2010

Abstract. We applied a ground-based vertically-pointing aerosol lidar to investigate the evolution of the instantaneous atmospheric boundary layer depth, its growth rate, associated entrainment processes, and turbulence characteristics. We used lidar measurements with range resolution of 3 m and time resolution of up to 0.033 s obtained in the course of a sunny day (26 June 2004) over an urban valley (central Stuttgart, 48°47' N, 9°12' E, 240 m above sea level). The lidar system uses a wavelength of 1064 nm and has a power-aperture product of 2.1 W m².

Three techniques are examined for determining the instantaneous convective boundary layer (CBL) depth from the high-resolution lidar measurements: the logarithm gradient method, the inflection point method, and the Haar wavelet transform method. The Haar wavelet-based approach is found to be the most robust technique for the automated detection of the CBL depth. Two different regimes of the CBL are discussed in detail: a quasi-stationary CBL in the afternoon and a CBL with rapid growth during morning transition in the presence of dust layers atop. Two different growth rates were found: 3–5 m/min for the growing CBL in the morning and 0.5–2 m/min during the quasi-steady regime. The mean entrainment zone thickness for the quasi-steady CBL was found to be ~75 m while the CBL top during the entire day varied between 0.7 km and 2.3 km. A fast Fourier-transform-based spectral analysis of the instantaneous CBL depth time series gave a spectral exponent value of 1.50 ± 0.04 , confirming non-stationary CBL behavior in the morning while for the other regime a value of 1.00 ± 0.06 was obtained indicating a quasi-stationary state of the CBL.

Assuming that the spatio-temporal variation of the particle backscatter cross-section of the aerosols in the scattering volume is due to number density fluctuations (negligible hygro-

scopic growth), the particle backscatter coefficient profiles can be used to investigate boundary layer turbulence since the aerosols act as tracers. We demonstrate that with our lidar measurements, vertical profiles of variance, skewness, and kurtosis of the fluctuations of the particle backscatter coefficient can be determined. The variance spectra at different altitudes inside the quasi-steady CBL showed an $f^{-5/3}$ dependency. The integral scale varied from 40 to 90 s (depending on height), which was significantly larger than the temporal resolution of the lidar data. Thus, the major part of the inertial subrange was detected and turbulent fluctuations could be resolved. For the quasi-stationary case, negative values of skewness were found inside the CBL while positive values were observed in the entrainment zone near the top of the CBL. For the case of the rapidly growing CBL, the skewness profile showed both positive and negative values even inside the CBL.

Keywords. Atmospheric composition and structure (Aerosols and particles) – Meteorology and atmospheric dynamics (Convective processes; Turbulence)

1 Introduction

Monitoring of the atmospheric boundary layer (ABL) is an important issue in atmospheric science since this layer is influenced by both the strength of land-surface exchange at the bottom and of entrainment processes at the top. These processes control the transport of particles, trace gases, and heat between the ground and the free troposphere (Stull, 1988).

The ABL depth is defined as the height of the inversion level separating the free troposphere (FT) from the boundary layer (e.g., Stull, 1988). This inversion layer is finite in depth, and thus covers a range of heights not a single discrete and strictly confined value. Furthermore, the entrainment near the top of the ABL is governed by complex processes



Correspondence to: S. Pal
(sandip.pal@uni-hohenheim.de)

and therefore, the ABL depth is variable on short time scales. According to Stull (1988), the ABL depth is defined as the “average height of the inversion base”. In contrast to this definition of a mean ABL depth, appropriate observational data with high temporal resolution allow to identify an instantaneous ABL depth and suggest studies on its variability.

The top of the ABL (here onwards referred as ABL height) can also be defined as the height of the minimum sensible heat flux. As long as passive scalars are accumulated in the ABL without the presence of any residual layer (RL) or aerosol layer (AL), large gradients of aerosol concentration or water vapor density occur at the inversion capping the ABL. These gradients are also suited for defining the top of the ABL (Stull, 1988). In ideal cases, the location of these gradients coincides with the minimum in the buoyancy flux profile (Sullivan et al., 1998). A sharp potential temperature jump also determines the ABL top (Boers et al., 1984). In consequence, the ABL height can be identified by characteristic features in profiles of several atmospheric variables. The most conventional method uses radiosonde-measured profiles of wind, temperature, and relative humidity (RH). It is noteworthy, that this approach yields a “snapshot”-view of the atmosphere. In contrast to radio soundings, active remote sensing systems are capable of providing continuous measurements of the key-variables of the atmosphere with high spatial and temporal resolution leading to better sampling statistics of the instantaneous ABL height. For this purpose, sodar (e.g. Beyrich and Gryning, 1998), radar wind profiler (e.g. Angevine et al., 1994), and lidar system (e.g. Russel et al., 1974) are in use. All these approaches have specific shortcomings and measurement uncertainties (Seibert et al., 2000).

In principle, determination of the ABL height with elastic backscatter lidar uses one of the following two methods: either a variance-based analysis through observation of mixing processes in the ABL or a gradient-based analysis of the vertical distribution of a passive tracer. For instance, the variance profile allows determining the mean convectively-driven atmospheric boundary layer (CBL) top height (henceforth referred as CBL height). The variance technique has been recently used by Lammert and Bösenberg (2006) to confirm the results of the logarithm gradient method (LGM), the most simple gradient approach. Also Martucci et al. (2007) compared the results obtained from LGM and the variance method but found that the mean CBL heights computed by LGM are statistically higher than the CBL heights computed by the variance method.

Previous lidar studies (e.g., Kiemle et al., 1997; Menut et al., 1999; Davis et al., 2000; Brooks, 2003; Wulfmeyer and Janjić, 2005; He et al., 2006) used one or two of three different gradient-based techniques for the ABL height determination: LGM, inflection point method (IP), and the Haar wavelet transform (HWT) scheme. In this article, we start the analyses with a comparison of CBL height retrievals via all three gradient-based techniques that have been used within

the literature so far and compare the results with higher-order moment analyses including variance-based method to determine the ABL height.

The comparison of LGM, IP and HWT is a worthwhile endeavor, since the various approaches used to determine CBL depth, generally produce slightly different results, and understanding of how they differ is necessary to compare different studies. To the best of our knowledge, no such study has been carried out yet. We apply these three techniques for the CBL height determination to very high resolution lidar measurements of 3 m and 0.33 s.

Once the evolution of the CBL height is determined with the best available approach, it is interesting to study whether these time series can help to quantify the non-stationarity involved. Major challenges lie in the application of a suitable approach to the problem of non-stationarities of the CBL height evolution. This arises due to the presence of vigorous thermal up- and downdrafts in this region. The CBL consists of highly fluctuating and irregular structures. Therefore, the top of the CBL is an implicative of this fluctuation. In order to quantify the aspects of variability and correlations at different temporal and spatial scales, fast Fourier transformation (FFT)-based power spectral analysis has been applied to the time series of instantaneous CBL height.

Smaller-scale processes often become important in the entrainment zone (EZ) due to high variability in the distribution of aerosol particles in these regions. The EZ is basically that region near the top of the boundary layer where vigorous mixing of the free-tropospheric air (by downdraft) and the thermals (by updraft) of the CBL occurs (Stull, 1988). Estimation of the entrainment zone thickness (EZT) therefore requires very high tempo-spatially resolved information of the tracers in this region. The instantaneous CBL height can significantly change within short time intervals especially when the convective activity is strong. The very high spatial resolution of lidar data yields an opportunity which is unique among all remote sensing techniques to capture small-scale features.

Turbulence in the CBL carries special signatures, which are of high importance for both atmospheric modeling concerning turbulence parameterization (Degrazia et al., 2000) and dispersion studies (Ulke, 2000). Turbulent mixing is considered to be the primary means by which aerosol particles and other scalars are transported vertically and produces fluctuations of concentrations. Statistical moments (variance, skewness, kurtosis, etc.) of these fluctuations describe the properties of the field of turbulent fluctuation and therefore are considered to be a fundamental tool in studying turbulence processes in the CBL. The vertical profiles of these higher-order moments then yield a description of the mixing processes at different heights in the CBL. As far as lidar measurements are concerned, previous studies have employed the profiles of the vertical velocity (e.g., Lenschow et al., 2000; Lothon et al., 2006), of water vapor mixing ratio (e.g., Wulfmeyer 1999a, b; Wulfmeyer et al., 2010), or of ozone

(Senff et al., 1996, among others) for investigating the turbulence features in the CBL. Recently, Engelmann et al. (2008) used lidar measurements of aerosol backscatter to estimate the aerosol flux in a CBL. However, in this study, the vertical profiles of higher-order moments of aerosol backscatter were not determined. The temperature gradient, which the definition of ABL height is based on, can be measured with rotational Raman lidar (Behrendt, 2005). Comparisons of LGM-determined CBL top values with such lidar-based temperature measurements have been presented by Radlach et al. (2008).

Statistical results of higher-order moments analyses of the particle backscatter signals inside the boundary layer are of high interest in order to explore the stochastic nature of turbulence. Indeed, these moments describe the tails of the probability density function; in particular, they provide the degree of the departure from a Gaussian form. The vertical profiles of these moments in the CBL provide further knowledge to foster our understanding about CBL turbulence features.

The aerosol lidar system of University of Hohenheim (UHOH) was installed in downtown Stuttgart to acquire data on four days from 23 to 26 June 2004. The primary objective for using the UHOH lidar was to obtain a close picture of the depth and variability of the CBL in this region and the consequent understanding of the CBL processes during different times of a day in summer. Such an experiment to explore the details of the CBL has not been made before in this area.

This paper is organized as follows. A brief description of the experimental site and meteorological conditions is given in Sect. 2. The set up of the UHOH lidar system is introduced in Sect. 3. The three gradient methods to determine the CBL height and the techniques to determine EZT and higher-order moments are outlined in Sect. 4. The results of the two cases are discussed in Sect. 5. A brief summary and an outlook are presented in Sect. 6.

2 The experimental site and meteorological conditions

The UHOH lidar system was deployed during the measurement period near the center of Stuttgart (48°46′43.5″ N, 9°10′48.9″ E, elevation approximately 240 m above sea level, a.s.l.) in southwestern Germany. The experimental site is located in a valley with complex topography. It is characterized by a large population density, high density of buildings, diverse anthropogenic activities, non-uniform land use, and enhanced industrial activities. Stuttgart is a major transportation cross point, including a large river port, an international airport, and a considerable industrial center. The orography of this city with the deepest point at the Neckar river of about 200 m a.s.l. and the highest point in Stuttgart-Vaihingen of about 550 m a.s.l. (just a few km away) influences the meteorological conditions.

Table 1. Technical parameters of the vertically-pointing UHOH elastic aerosol lidar system.

Transmitter	
Nd:YAG laser	
Wavelength:	1064 nm
Pulse energy:	600 mJ @ 1064 nm
Pulse repetition rate:	30 Hz
Pulse duration:	10 ns
Power aperture product:	2.12 Wm ²
Telescope	
Type:	Ritchey-Chretien (Astro Optic)
Diameter of primary mirror:	40 cm
Diameter of secondary mirror:	10 cm
Focal ratio:	f/10
Coating:	Aluminum with quartz protective coating
Detectors	
Si-APD for 1064 nm and PMT for 532 nm	
Analog-to-digital converter	
Compu-Scope	14 100
Analog-to-digital resolution:	14 bits
Sampling rate:	50 Ms/s (for 2 channels)
Sampling in range:	3 m

During the measurement period, the sky was mostly cloud-free. As to weather conditions, absolute maximum temperature of 25.5 °C, absolute minimum of 9.5 °C, maximum RH of 78.4% and minimum of 16.2% RH at ground, only fair weather cumuli, some thin cirrus clouds and no precipitation were observed during the measurement period. The mean wind speed at 10 m height was 3–4 ms⁻¹. This meteorological dataset was collected by the weather station in Stuttgart City (Amt für Umweltschutz der Stadt Stuttgart, Schwabenzentrum-Stadtmitte, at 48°46′20″ N, 9°10′46″ E, 275 m a.s.l.) about 500 m distant from the lidar site. The surface temperature on 26 June 2004 reached its maximum value of 25.5 °C at 16:30 CEST (central European summer time, UTC+2 h). Horizontal wind obtained at 10 m height was mild (1–1.5 ms⁻¹). The RH at ground showed a classical diurnal cycle with a maximum RH of about 80% at around 06:00 CEST and minimum RH of 30% at 17:00 CEST on 26 June 2004. The UHOH lidar continuously monitored the CBL for more than eight hours on this day. Consequently, within this study, we decided to use the lidar measurements obtained on this day.

3 Experimental set up of the lidar system

The elastic lidar system of UHOH was operated in an intermediate configuration on the way to a scanning lidar system

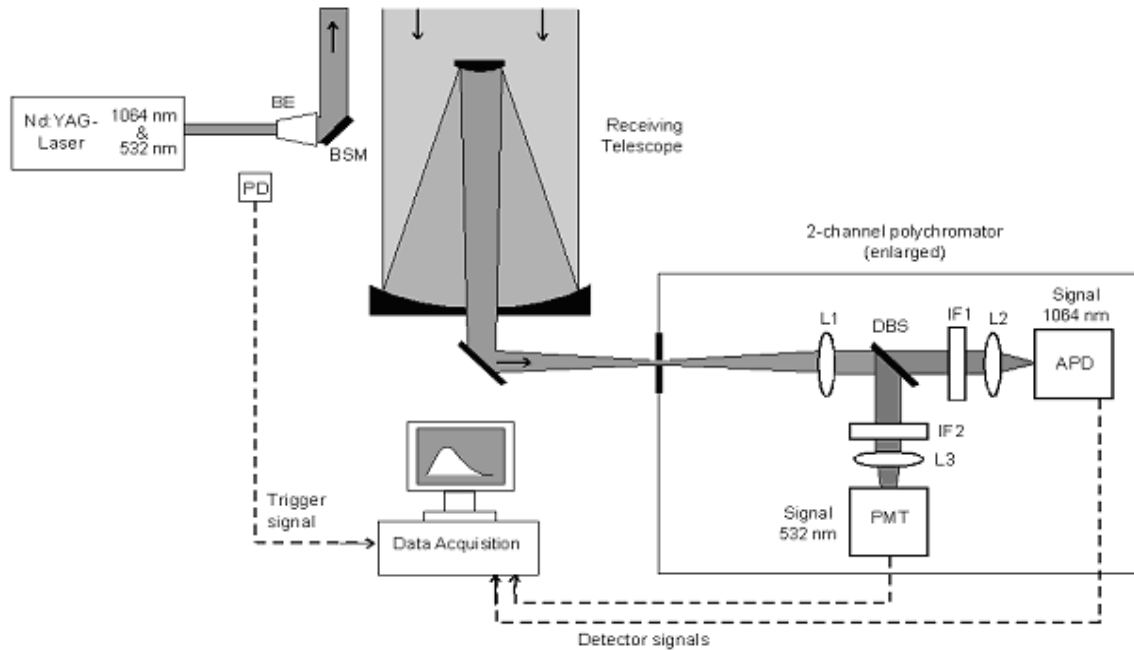


Fig. 1. Scheme of the elastic backscatter lidar of UHOH. APD: Avalanche photodiode, BE: Beam expander, BSM: Beam steering mirror, DBS: Dichroic beam splitter, IF1–IF2: Interference filters, L1–L3: Lenses, PMT: Photomultiplier tube, PD: Photodiode.

for aerosol and temperature measurements (Behrendt et al., 2005; Pal et al., 2006, 2010; Radlach et al., 2008).

This version of the lidar system worked in monostatic vertically-pointing biaxial configuration with a maximum spatial and temporal resolution of 3 m and 0.033 s, respectively. The lidar system was equipped with a flash-lamp-pumped Nd:YAG laser emitting simultaneously the fundamental and the second harmonic wavelengths of 1064 nm and 532 nm, respectively. Pulses of ~ 10 ns duration with a pulse energy of 600 mJ at both wavelengths were transmitted. The schematic set-up and specifications of the lidar system are shown in Fig. 1 and Table 1, respectively.

The backscattered light was sampled with a Ritchey-Chretien-type telescope with a 40-cm-diameter primary mirror. The backscattered light passed a lens and was then split by a dichroic beam splitter, separating the signals of the two transmitted wavelengths. The two beams were analyzed by means of two interference filters, both with 5 cm diameter and 10 nm half-width-at-half-maximum (HWHM) band-pass before reaching the detectors: a photomultiplier tube (PMT, Hamamatsu R7400-U02) for 532 nm and a silicon avalanche photodiode (Si-APD, Perkin & Elmer C3095E) for 1064 nm. The diameter of the sensitive area of the APD and the PMT were 0.8 mm and 8 mm, respectively.

The data acquisition system stored the lidar data with a frequency of 30 Hz, i.e., for each laser pulse. The data acquisition and processing unit was comprised of a two-channel Gage CS 14100 card with 14 bit resolution analog-to-digital converter sampling the backscattered signal with 50 MHz to

provide data with 3 m vertical resolution, and a standard personal computer. It processed the lidar data using an automated LabView code and then stored on a hard disk. The vertical profiles of the raw and the range-square-corrected backscatter signal and time-versus altitude images of the lidar signal were displayed in real time.

4 Methods

4.1 Determination of the atmospheric boundary layer height

4.1.1 Lidar equation

The monostatic elastic lidar signal is expressed as

$$P_{\lambda}(R) = P_{0,\lambda} \frac{c t_p}{2} K_{\text{eff}} \frac{A}{R^2} O(R) \beta_{\lambda}(R) \exp\left(-2 \int_0^R \alpha_{\lambda}(r) dr\right). \quad (1)$$

where $P_{\lambda}(R)$ is the received signal intensity at the wavelength λ from range R , $P_{0,\lambda}$ is the laser peak power, c is the velocity of light, t_p is the laser pulse duration, K_{eff} is the overall efficiency of the lidar system, A is the receiving area of the telescope, $O(R)$ is the laser-beam receiver-field-of-view overlap function, $\beta_{\lambda}(R)$ is the total backscatter coefficient due to atmospheric particles and molecules, and $\alpha_{\lambda}(R)$ is the total extinction coefficient due to atmospheric particles and molecules. If the aerosol extinction is small,

at 1064 nm, the range-square-corrected backscatter signal intensity is approximately proportional to the particle backscatter coefficient ($\beta_{\lambda, \text{par}}$); the Rayleigh scattering due to the atmospheric molecules at this wavelength is nearly negligible. In this case, Eq. (1) can be approximated as

$$P_{\lambda}(R) R^2 \cong C \beta_{\text{par}}(R). \quad (2)$$

where C is a constant and $\beta_{\text{par}}(R)$ is the particle backscatter coefficient at wavelength λ .

4.1.2 Logarithm gradient method

The first approach adopted here for determining the ABL height is based on the calculation of the vertical gradient of the logarithm of the range-square-corrected lidar backscattered signal (Senff, 1996; Wulfmeyer, 1999a). This gradient is expressed as

$$D(z) = \frac{d(\ln(P(z)z^2))}{dz} \approx \frac{\ln(P(z_2)z_2^2) - \ln(P(z_1)z_1^2)}{z_2 - z_1} \quad (3)$$

where z_2 and z_1 are two different heights ($z_2 > z_1$ and $z = (z_2 + z_1)/2$) from the lidar. Please note that range R is replaced here and in the following by height z as we discuss vertically-pointing lidar measurements. The use of the derivative of the logarithm of range-squared corrected signal yields one advantage compared to the use of the derivative of only the range-squared corrected signal. The benefit is to have the extinction coefficient (although small) in linear form allowing maxima and minima to appear with higher contrast.

The lidar signal generally shows a local discontinuity between the mixed layer and the FT above, more or less well marked, depending on turbulent activity and aerosol distributions. The altitude corresponding to the minimum of $D(z)$ is taken as the instantaneous ABL top. This height is denoted throughout the text and in figures as z_{LGM} and is expressed as

$$z_{\text{LGM}} \equiv \min(D(z)) \quad (4)$$

When high-resolution lidar datasets are used, several minima may exist in $D(z)$ complicating the selection of the appropriate peak which corresponds to the CBL top. Therefore, special care should be taken in the averaging scheme before the LGM is applied.

4.1.3 Inflection point method

The ABL height determination by IP method (Menuet et al., 1999) is performed by identifying the altitude corresponding to the minimum of the second derivative of the logarithm of the range-square-corrected signal which gives

$$z_{\text{IP}} \equiv \min \left[\frac{d^2(\ln(P(z)z^2))}{dz^2} \right]. \quad (5)$$

This definition is different from the LGM. The IP method searches for the altitude where the inflection point of $D(z)$

occurs. z_{IP} is in general lower than z_{LGM} since the second derivative changes its sign each time the first derivative changes direction. The second derivative function exhibits various minima below and above z_{LGM} . In this regard, Sicard et al. (2006) demonstrated that the best estimator with the IP method is the minimum of the second derivative located just below z_{LGM} . We follow this concept.

4.1.4 Haar wavelet transform method

The Haar wavelet function, which is the most simple orthogonal mother-wavelet function (Daubechies et al., 1992), has been used by many authors for determining the ABL height (e.g. Davis et al., 2000; Cohn and Angevine, 2000; Brooks, 2003). The Haar wavelet function returns large coefficient values where a profile has large gradients.

The Haar wavelet is defined as

$$H\left(\frac{z-b}{a}\right) = \begin{cases} 1 & \text{for } b - a/2 \leq z \leq b \\ -1 & \text{for } b < z \leq b + a/2 \\ 0 & \text{otherwise} \end{cases} \quad (6)$$

where z is height and a and b are the dilation and translation of the wavelet, respectively.

For a function $f(z)$ (here, range-corrected lidar signal $P(z)z^2$) and the Haar wavelet H , the convolution, $W_f(a, b)$ is defined as the covariance transform (Gamage and Hagelberg, 1993). After normalization with the dilation value, this function reads

$$W_f(a, b) = \frac{1}{a} \int_{z_{\text{min}}}^{z_{\text{max}}} \left\{ P(z)z^2 H\left(\frac{z-b}{a}\right) \right\} dz. \quad (7)$$

An advantage of using a normalization factor a^{-1} instead of $a^{-1/2}$ is that sharp transitions can easily be detected (Gamage and Hagelberg, 1993). z_{min} and z_{max} are the lower and upper altitude of the lidar profile, respectively, between which the HWT is applied. The maximum value of the covariance transform corresponds to the strong step-like decrease in backscatter signal. The corresponding altitude of the resulting maximum is identified as the ABL top and is expressed as

$$z_{\text{HWT}} \equiv \max(W_f(a, b)) \quad \text{for } z_{\text{min}} < b < z_{\text{max}} \quad (8)$$

This technique works well except for complicated cases, e.g., when the boundary layer consists of the newly developing CBL and one or more RL (steep inversion) in the lower troposphere possibly in the morning. However, no vertical averaging in the lidar profiles is necessary like for the LGM.

4.2 Estimation of entrainment zone thickness

The existence of different entrainment regimes and hysteresis effects in the daytime evolution of the EZ makes the retrieval of EZT complicated (Flamant et al., 1997). The top of the EZ can be easily determined, but the bottom of the EZ is not well

defined. The bottom of the EZ is characterized by an altitude where 5–10% of the air has FT characteristics. In this study we use this definition to estimate EZT.

EZT can be determined from cumulative frequency distribution of the instantaneous CBL height measurement by lidar (e.g., Stull and Eloranta, 1984; Melfi et al., 1985). This technique estimates the height differences between the 5–10% and 90–95% values of the cumulative frequency distributions of instantaneous CBL height evolution. Melfi et al. (1985) considered lower and upper limits of the cumulative frequency distribution to be 4% and 98%, respectively. In contrast to this, Flamant et al. (1997) and Beyrich and Gryning (1998), mentioned that the choice of a fixed percentage value is rather complicated due to intense mixing in the EZ (both horizontally and vertically). Therefore, the average values of the 5–10% values were considered for minimizing the possible step effects in the frequency distribution.

Our analysis is not directly comparable with that of Melfi et al. (1985). They considered the EZ in a spatially averaged sense whereas we take into account the EZ in a time averaged sense. EZT is computed here from the time series from a vertically-pointing ground-based lidar while most studies including Melfi et al. (1985) have used spatial series of downward looking lidar from aircraft. It is assumed in our case that the EZ is “a measure of the averaged vertical size of the ABL-height fluctuations” as defined in Boers et al. (1995). It should be mentioned here that Taylor’s “frozen turbulence” hypothesis could be used to transform temporal data into the spatial domain (Taylor, 1921). These results are then compared with the standard deviation approach (Davis et al., 1997; Schwemmer et al., 2004).

4.3 Procedure for higher-order moments estimation

For the retrieval of statistical moments, it is assumed that fluctuations (both in time and height) of the backscatter coefficient in the CBL are mainly due to changes of total aerosol number density or mass but not due to the fluctuations of the microphysical properties of the aerosol particles. The latter may be due to aerosol swelling particularly true for high RH for which the hygroscopic growth of aerosols is more pronounced (Hänel, 1976) and advection of different particle types. Variability of the aerosol backscatter in the EZ may be significant due to aerosol swelling in this region (Wulfmeyer and Feingold, 2000; Gibert et al., 2007).

According to the Mie theory (Bohren and Huffman, 1983), the particle backscatter coefficient at a certain height z can be expressed as

$$\beta_{\lambda, \text{par}}(z, t) = \sum_{i=1}^N \int_0^{\infty} Q_{\text{bsc}, \pi, i, z, t}^{\text{par}}(r, m, \lambda) \pi r^2 n_{i, z, t}(r) dr \quad (9)$$

$Q_{\text{bsc}, \pi, i, z, t}^{\text{par}}(r, m, \lambda)$ stands for the backscatter efficiency at the lidar wavelength λ , r is the particle radius and m is the complex refractive index of the particle, $n(r)$ is the number of

particles with radius r . The index i in Eq. (9) describes various particle types.

If one neglects the variation of the aerosol size with the relative humidity and assumes similar types of aerosol particles in the study region, then the fluctuation of $\beta_{\lambda, \text{par}}(z)$ can be expressed as

$$\beta_{\lambda, \text{par}}(z) \approx \int_0^R \overline{Q_z}(r, m, \lambda) \overline{n_z}(r) \pi r^2 dr \quad (10)$$

Now, we introduce the assumption that the fluctuations of the aerosol microphysical properties are significantly smaller than the fluctuations of the total number density in the observed volume of the lidar. In this case,

$$\beta_{\lambda, \text{par}}(z, t) \approx N_{0, z}(t) \int_0^R \overline{Q_z}(r, m, \lambda) \frac{\overline{n_z}(r)}{N_0} r^2 dr \approx N_{0, z}(t) C(z) \quad (11)$$

Under these assumptions, the fluctuation in the range-square corrected backscatter signal and hence in $\beta_{\text{par}}(t)$ at a certain height z is approximately proportional to the fluctuations in the aerosol number density at that height as shown below,

$$\beta'_{\text{par}}(t) \sim N'(t) \quad (12)$$

where $N'(t)$ is the fluctuation of the number density and

$$\frac{\beta'_{\text{par}}(t)}{\beta_{\text{par}}(t)} \approx \frac{N'(t)}{N(t)}. \quad (13)$$

Furthermore, the relative fluctuation of the backscatter coefficient becomes equal to the relative fluctuation of the aerosol number density. Under similar assumptions, Engelmann et al. (2008) showed the variability of the aerosol mass flux in a CBL.

Profiles of higher-order moments of fluctuations of the aerosol backscatter intensity i.e., variance V , skewness S_k , and kurtosis K are derived here following the methods introduced by Lenschow et al. (2000). During the error analysis, the system noise errors and the sampling errors were considered. The techniques for the determination of these noise terms were extensively discussed in Senff et al. (1994) and Wulfmeyer (1999a). Using the noise error profiles by means of statistical error propagation, variance, skewness, and kurtosis profiles including error (with respect to statistical and sampling errors) were determined. Autocovariance analyses of the high-resolution time series and analyses of variance spectra were performed for this purpose.

5 Results and discussion

The vertically-pointing UHOH aerosol backscatter lidar provides two-dimensional observations of the lower troposphere. During measurements in downtown Stuttgart, the

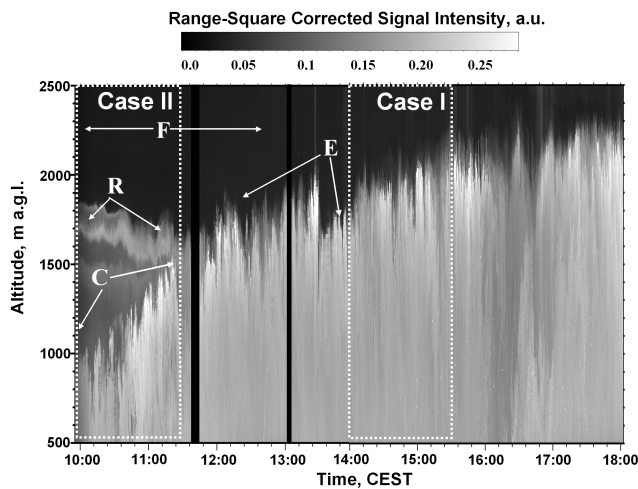


Fig. 2. Time-height cross-section of the range-square-corrected backscatter signal measured on 26 June 2004 from 09:55 to 18:10 CEST. Dotted boxes are the selected regions of Case I and Case II. Temporal and spatial resolutions are 0.033 s and 3 m, respectively. R: a strong residual layer from previous day showed up around 1.8 km a.g.l., F: free atmospheric air with very low aerosol load above 2.0 km a.g.l., C: CBL growth during morning eroded the nighttime stable residual layer, E: entrainment at the top of the CBL. Black stripes mark two gaps where no data are available.

UHOH lidar system collected data up to 12 km above ground level (a.g.l.). Figure 2 depicts the time-height cross-section of an eight hour observation of the background-subtracted and range-square-corrected signal in the 1064-nm channel collected between 09:55 and 18:00 CEST on 26 June 2004.

The data is plotted with the maximum resolution possible by the present system, i.e., a time resolution of 0.033 s and a vertical resolution of 3 m. Small-scale turbulent activity in the CBL is clearly visible. This figure demonstrates the UHOH lidar's capability to observe the boundary layer with ultra-high resolution and to provide a detailed view on fine structures of the aerosol distributions.

The time-height cross-section shows that a previous night RL marked by "R" was present at altitudes between 1.6 and 1.7 km in the morning until 11:20 CEST while the free-tropospheric air with very low aerosol load was present above 2.1 km altitude (marked by "F"). The RL is the previous day's mixed layer that the new CBL grows into, and as such lies immediately above the CBL. There is also a very thin AL above the RL at an altitude of 1.8 km (see Fig. 2, a separate, third layer above the RL). Around 11:30 CEST, the growing CBL (marked by "C") reached the level of the RL merging with it so that both became indistinguishable. Such overshoots are considered to be caused by the initial development of large convective rolls, which turn into more random motions after the quasi-steady equilibrium. Also visible is that starting at 11:20 CEST, the dust layer became trapped in the entrainment region (marked by "E"). This is called penetra-

tive convection (Deardorff et al., 1969). As a result of this activity, cleaner air from the FT enters the CBL by downdrafts. The RL at 1.6 km a.g.l. in the present case was also observed in the lidar data collected on the previous night (not shown here). Influenced by this process, the CBL grew in thickness and thus a one-way entrainment dominated. When laminar air from the FT and capping inversion are introduced into the CBL, the thickness of the CBL grows. On the contrary, none of the turbulent air is incorporated into the laminar air of the FT. These characteristics were clearly observed by the UHOH lidar measurements.

Between 12:00 and 18:00 CEST, the height of the CBL remained nearly constant around 2.0 km a.g.l. In summary, we found two different regimes of the CBL evolution: one during the rapid growth of the CBL until 12:00 CEST and one in the afternoon with equilibrium entrainment i.e., when CBL evolution is in a quasi-steady state. The quasi-stationary CBL (referred to as Case I in the following) is used first to demonstrate the three techniques for CBL height as well as higher-order moments determination. These analyses were then extended to study the CBL in the morning (Case II).

5.1 Case I: Quasi-stationary convective boundary layer

5.1.1 Results obtained with logarithm gradient method, inflection point method, and Haar wavelet transform analysis

Figure 3 illustrates the retrieval of z_{LGM} , z_{IP} , and z_{HWT} for backscatter signals acquired at 15:52 CEST on 26 June 2004. Before the LGM, IP, and HWT were applied to the lidar data, 10 consecutive lidar profiles were averaged which provided a time resolution of 0.33 s.

In the following analysis for LGM and IP method, no further time averaging was performed. Instead, a gliding average with a Gaussian window of full width at half maximum of 30 m was applied in height to the stored lidar profiles before $D(z)$ was calculated. This averaging was necessary to determine the minimum gradient peak. The influence of changing height difference ($dz=z_2-z_1$) on $D(z)$ was tested. After performing this sensitivity test, the appropriate peak in the $D(z)$ profile related to the ABL top was found. For these data, dz of 30 m was found to be most appropriate for searching the minimum of $D(z)$.

Figure 3 clearly shows that the minimum of the 2nd derivative (inflection point, panel c in figure) appears below the height of the minimum of the 1st derivative (panel b). z_{IP} is always lower than z_{LGM} because the 2nd derivative of the range-square-corrected signal has always a local log-minimum below the minimum of the 1st derivative. The IP method searches for the interface between the mixed layer and the FT and therefore z_{IP} marks the middle of the transition zone. The LGM identifies the location of the minimum in the vertical gradient of the backscatter, which tends to lie within the upper part of the transition zone. This directly

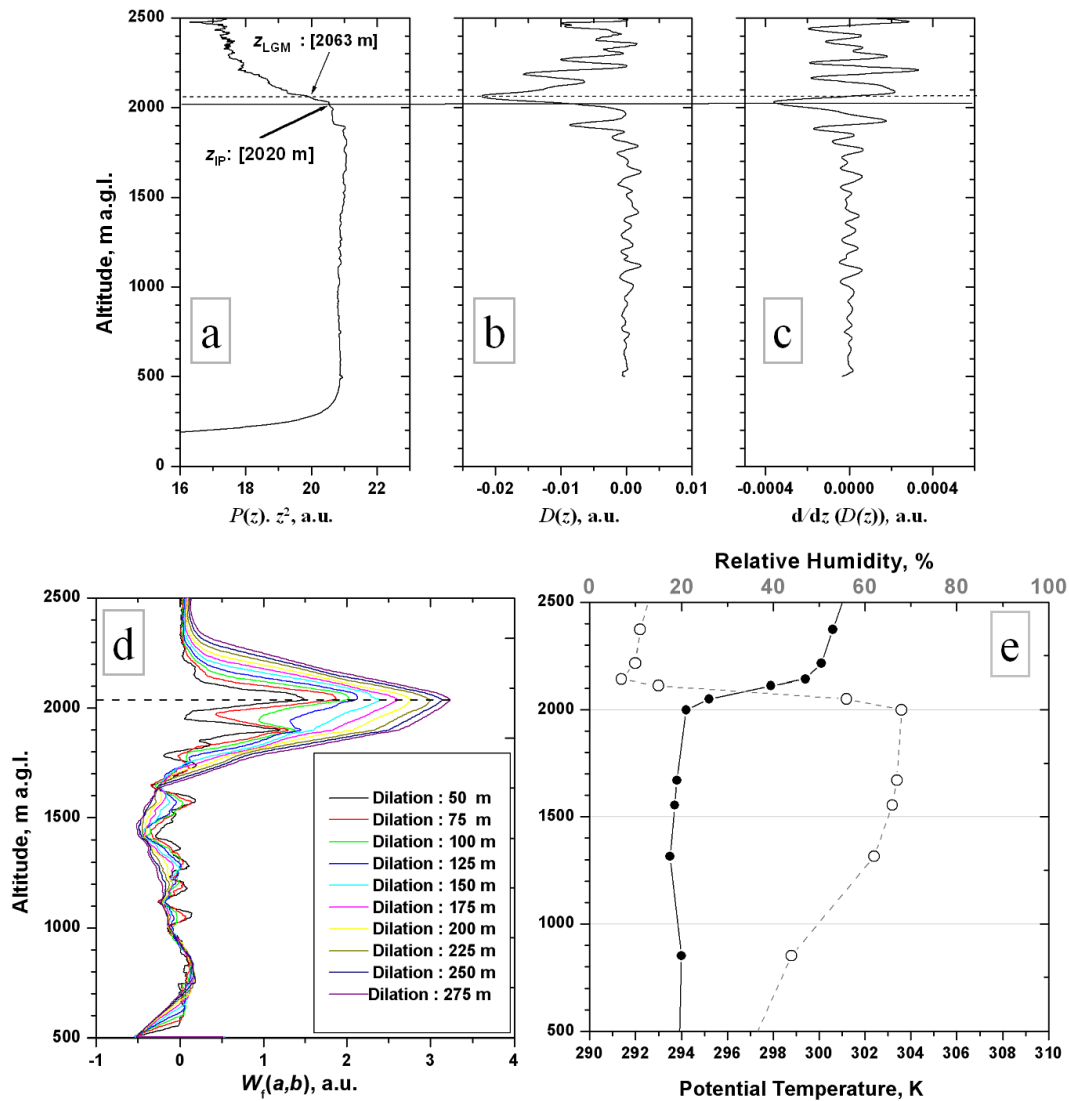


Fig. 3. Determination of the instantaneous height of the CBL on 26 June 2004 at 15:52 CEST using LGM, IP method, and HWT-based approach. (a) the background-subtracted range-square corrected backscatter signal, (b) the 1st derivative of its logarithm, (c) the 2nd derivative. The temporal and spatial resolution of the data is 0.33 s and 3 m, respectively. In height, a 30 m gliding average is applied. z_{LGM} and z_{IP} are found at 2063 m and 2020 m a.g.l., respectively. (d) Wavelet covariance transform $W_f(a,b)$ values for different dilations from 50 m to 275 m. For dilations greater than 175 m, $W_f(a,b)$ shows a clear maximum at 2030 m. (e) Profiles of the potential temperature (bold dots with solid line) and relative humidity (dashed line) obtained from the radiosonde launch at 14:00 CEST from Schnarrenberg, Stuttgart (48.8333° N, 9.2000° E, 315 m a.s.l.) on 26 June 2004.

implies $z_{LGM} > z_{IP}$ (Figs. 3 and 4). Depending upon the turbulent activity present in the CBL, the local discontinuity between CBL and FT atop is defined as the transition zone here. This transition zone is also a means of determining the EZT in different atmospheric conditions (Sect. 4.2).

The HWT-based analysis was applied to the same data to determine the CBL height. The wavelet covariance transform $W_f(a,b)$ was computed for each profile and the altitude corresponding to its maximum was denoted as the CBL top. The crucial point for estimating CBL height following this approach is dependent on the choice of two parameters:

the interval between upper (z_{max}) and lower (z_{min}) altitude where the HWT should be applied, and the values of the dilation a and translation b . Following Davis et al. (2000), a sensitivity test was performed to obtain the characteristic differences of $W_f(a,b)$ for different dilations as shown in Fig. 3 (panel d). The location of the maximum covariance turned out to be at an altitude of 2030 m for $a > 175$ m. The dilation values lower than 175 m exhibited two or three peaks in the $W_f(a,b)$ function making the determination of z_{HWT} questionable. For obtaining z_{HWT} , the dilation value of 200 m was chosen for the complete time series of Case I. Unless

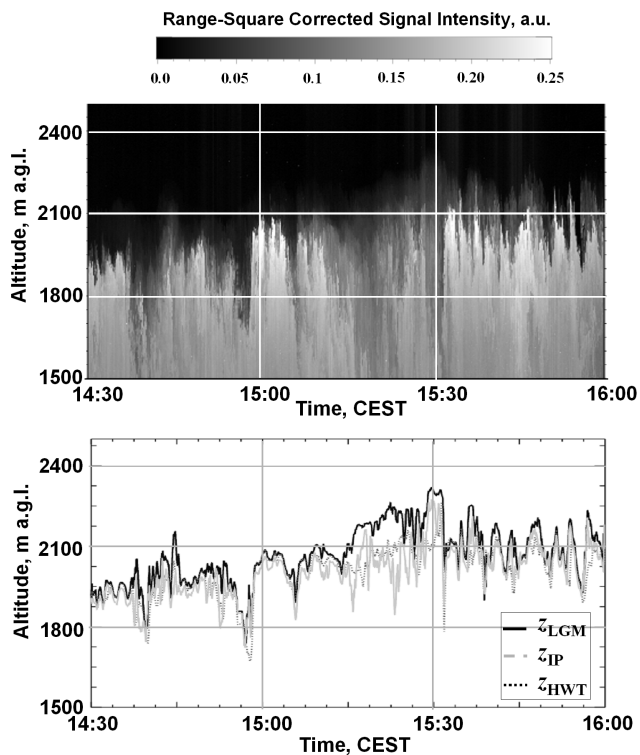


Fig. 4. Zoom-in-view of the time-height cross-section of range-square corrected signal during Case I (upper panel) and the time series of z_{LGM} , z_{HWT} , and z_{IP} (lower panel).

otherwise stated, the HWT analysis was constrained between the heights of 500 and 3000 m a.g.l.

The HWT coefficient becomes maximal when the covariance between backscatter profile and the Haar function is maximum. Brooks (2003) showed how the HWT method identifies a point close to the center of the transition zone, with a trend towards higher values with increasing dilation. Thus, HWT method will tend to identify a point lower than the LGM, though the difference will vary both from profile to profile and with dilation for any given profile. This issue is further extended in the next section.

5.1.2 Intercomparison between the different techniques

Figure 4 presents the time-height cross-section of the range-square corrected signal intensity (upper panel) collected between 14:30 and 16:00 CEST and the temporal evolution of z_{LGM} , z_{IP} , and z_{HWT} (lower panel). The two time series using the LGM and the HWT are highly correlated and the linear trends in both cases are very similar. Correlation analyses among the three time series were performed. The resulting correlation coefficients between time series of z_{LGM} and z_{HWT} , z_{LGM} and z_{IP} , and z_{IP} and z_{HWT} are 0.851, 0.811, and 0.781, respectively. In general, z_{HWT} is lower than z_{LGM} .

It is important to mention here that the LGM and the HWT analysis become the same as soon as a dilation equal to the

range resolution (in this case 3 m) is applied in the HWT analysis. The HWT method allows limiting the analysis to a chosen range of scales, so that small scale gradients (e.g., caused by noise) do not appear. The HWT coefficient is calculated at each height level; caused by this implicit smoothing, the technique does not require additional averaging of the signals in height as in the case of the LGM.

Comparison of the mean CBL heights determined from the respective time series yielded a difference of 59 m between the LGM and the HWT-based analysis while a difference of 63 m was found between LGM and IP method. A difference of only 4 m was found when comparing the mean CBL heights estimated by the HWT and IP method.

It is further important to note that the CBL height determined by HWT is in better agreement with the results of the variance profiles (see Sect. 5.5) than the other two techniques. Also the “snapshot” view provided by the radiosonde launch at 12:00 UTC on this day from the near-by weather station (Schnarrenberg, Stuttgart) confirmed this fact. We estimate the top of the CBL by calculating the first derivative of the potential temperature ($d\theta/dz$, where θ is the potential temperature) obtained from the radiosonde. The radiosonde measurements revealed a strong signature of the temperature inversion and a sharp drop in the RH at an altitude of 2005 m a.g.l. confirming the mean CBL height of $z_{HWT}=2008$ m (panel e in Fig. 3). In contrast to this, the LGM-based results do not show such close similarity neither with the variance profile nor with the radiosonde-derived CBL height.

The application of LGM often becomes quite complicated because the minimum may alternate between largely separated values over an extended height range. In contrast to this, the HWT-based approach being a convolution does not show several peaks in the distribution of the HWT coefficient, in case an appropriate dilation value is selected. Previous studies on the application of the HWT method used relatively high values of dilation (of about 450 m in Baars et al., 2008; of about 1000 m in Cohn and Angevine, 2000). The high spatial resolution of the UHOH lidar data in combination with high signal-to-noise ratio is the reason for using a relatively low dilation value of 200 m while the high temporal resolution facilitated to obtain a detailed view on the significant temporal variability of CBL height. Indeed, calculation of wavelet coefficients with a large dilation has some disadvantages in determining CBL height. Larger dilations would require unnecessary computations and are more susceptible to errors from a varying backscatter profile above the CBL, particularly if there are various layers, as it will be discussed later (Sect. 5.2). Influence of the boundary effects increases for large dilations. Boundary effects occur at altitudes that are less than one wavelet dilatation from a boundary (the lowest or highest available data) where the convolution is not well defined. Furthermore, for a sloped aerosol backscatter within the CBL or free atmosphere, large dilation values will provide a huge uncertainty in the calculation

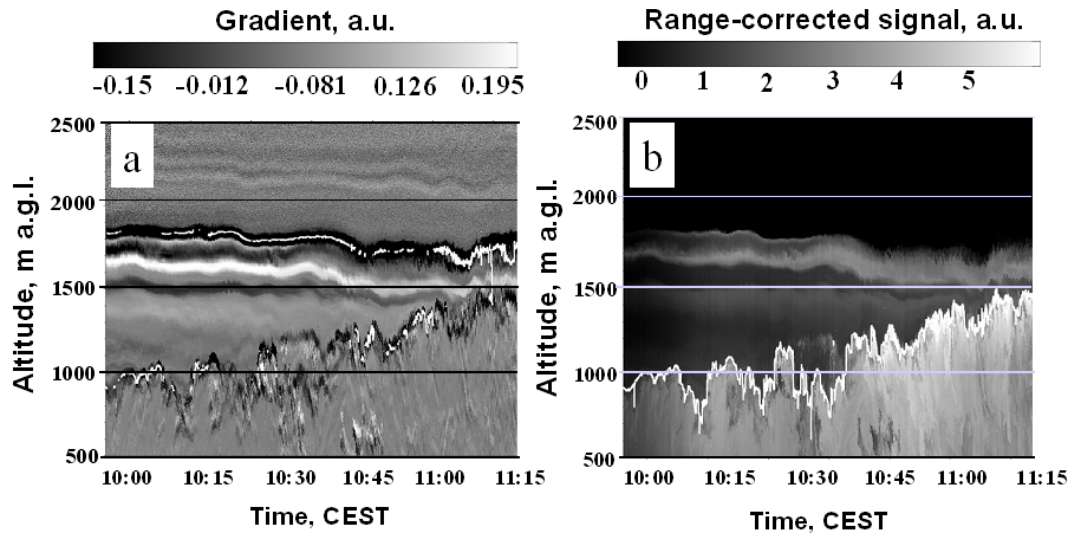


Fig. 5. Retrieval of z_{HWT} in the presence of several aerosol layers in the CBL during Case II. The HWT has been applied in the altitude range of 500 m to 3000 m with a dilation value of 260 m. **(a)** time-altitude-plot of $D(z)$. A broken white line marks the location of the maximum of $W_f(a,b)$. The HWT-based method mostly identifies erroneously the residual aerosol layer height as ABL top in this case. **(b)** HWT is applied in selected altitudes. The upper limit has been restricted to below the residual aerosol layer. Time series of CBL top z_{HWT} (white solid line) superimposed on the range-square corrected lidar backscatter intensity. The convectively growing ABL top is identified correctly and is consistent with a strong gradient in the entrainment zone.

of wavelet coefficient. A sloped aerosol backscatter arises due to the changes in aerosol microphysical properties or aerosol concentrations. This is an important source of bias with the wavelet method. Most probably, a difference of around 100 m between the z_{LGM} and z_{HWT} are observed around 15:15 CEST for this reason (Fig. 4, lower panel). A large transition zone during this period can also be seen in the time-height cross-section.

The IP method uses the results from LGM and a number of criteria have to be fulfilled to obtain z_{IP} as a correct estimate of CBL height (see Sicard et al., 2006, for a detailed discussion on these criteria).

In summary, it can be stated that z_{LGM} tends to fall within the upper part of the transition zone, z_{HWT} close to the middle, and z_{IP} near the bottom ($z_{\text{LGM}} > z_{\text{HWT}} > z_{\text{IP}}$). We conceive that this is a characteristic difference among the techniques. It is important to note that for the first time we have compared three different algorithms to find the CBL height from a very high-resolution lidar measurements: 8 h of observation were used for this purpose. Similar differences among the techniques were found for the rest of the time series although not shown here.

Furthermore, it is important to note that the inversion which defines the top of the boundary layer is a thermodynamic feature. Lidar backscatter is assumed to reflect the thermodynamic inversion closely because it is approximately proportional to the aerosol concentration, which is generally well mixed within the CBL, much lower in concentration in the FT, and thus has a transition that closely

matches the inversion. Aerosol size, however, is a function of humidity, which often falls dramatically across the inversion layer. Therefore, the lidar backscatter is thus not truly conserved and differences between the transition zone limits of lidar backscatter profile and thermodynamic inversion might exist, at least for some conditions. However, it can be concluded that the HWT-based approach is the most suitable and preferable technique for the determination of the instantaneous CBL height; limitations certainly exist as some subjective approach has to be applied for lidar data collected during complex situations (as will be shown in the very next section).

5.2 Case II: Convective boundary layer height during its rapid growth in the morning

This section deals with the investigation of CBL evolution between 09:55 and 11:15 CEST on the same day. During this time, the CBL transformed from a stratified structure in the morning to a well-mixed CBL toward noon.

The application of the HWT-based method can lead to significant problems when multiple aerosol layers exist like during Case II. The other two methods also have similar biases. Figure 5a is the time-height plot of $D(z)$. The RL and the AL were confined within altitudes from 1.6 to 1.8 km. The LGM picked the strongest gradient, which was not always at the top of the newly developing CBL but for many profiles was found in the region of the RL and the AL. Thus a fully automated LGM routine fails to identify the top of the CBL. The HWT was applied within altitudes from 500–3000 m.

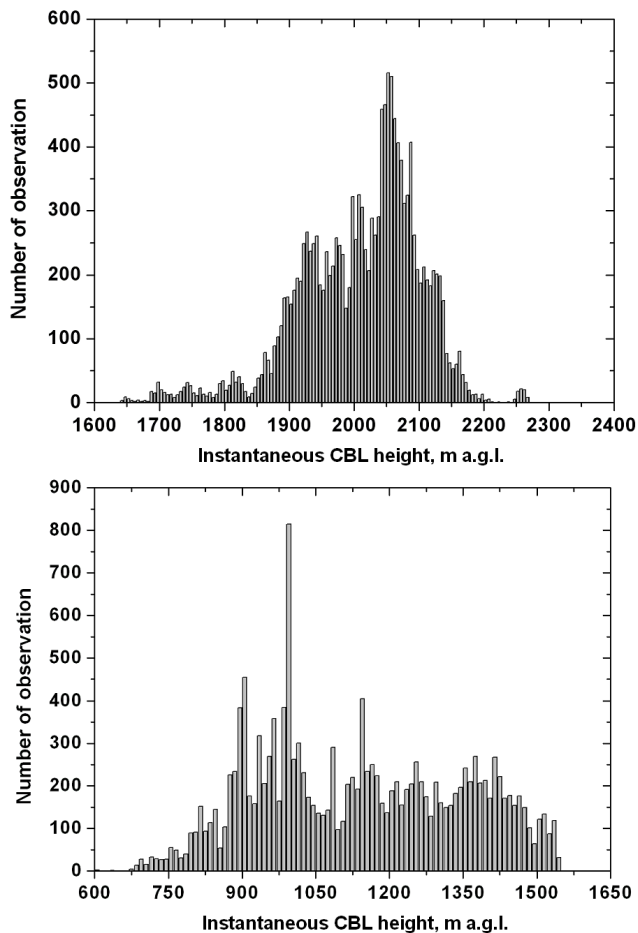


Fig. 6. Frequency distribution of the instantaneous CBL height derived by the HWT-based method for Case I (top) and Case II (bottom).

A similar analysis was performed for the choice of dilation value as in Case I. A dilation value of 260 m was found suitable for this dataset. It was mentioned earlier that the value of most suitable dilation depends on the nature of backscatter profile. Figure 5a displays that HWT most of the times picked the top of the RL and sometimes AL instead of the top of the convectively growing boundary layer.

The HWT analysis was modified with the following procedure. At first, the aerosol layer was identified from the time-versus-altitude plot of $D(z)$ as displayed in Fig. 5a. Then the upper altitude limit below the aerosol layer was selected and used as z_{\max} (in Eq. 7). The upper limit in the integration for obtaining the $W_f(a, b)$ is now not constant but varies in time. Following this subjective approach (Senff et al., 2002), difficulties arising due to the appearance of RL and AL were eliminated. Figure 5b shows the growth of CBL top (white solid line) overlaid on the range-square-corrected backscatter intensity after the subjective approach was applied. The morning time convection is seen clearly in both figures with the growing CBL top from 0.7 to 1.5 km.

5.3 Entrainment zone thickness for two cases

Two different approaches were studied for estimating the EZT from the time series of z_{HWT} . First, the standard deviation of z_{HWT} is used (e.g., Davis et al., 1997). This technique assigned here as the standard deviation technique provided an estimate of the mean EZT: 92 m and 185 m for Case I and Case II, respectively. The frequency distributions of z_{HWT} for both cases are shown in Fig. 6. For Case I (upper panel), the distribution is slightly asymmetric around 2050 m a.g.l. and does not spread much. Larger values are considered to be due to the most energetic thermals. The values around 1700 m a.g.l. were arising mostly during a strong entrainment of free-tropospheric clean air. On the other hand, for Case II, the frequency distribution is highly asymmetrical reflecting an entirely different regime of the CBL (lower panel of Fig. 6). The broader distribution is due to the fact that z_{HWT} is increasing from 900 m to 1500 m in Case II.

Results obtained with the cumulative frequency distribution method are shown in Fig. 7. This figure shows the evolution of z_{HWT} with an illustration of the technique on the time series for both cases. Lower and upper parts of the EZ are denoted as $z_{\text{HWT}(05/10)}$ and $z_{\text{HWT}(90/95)}$, respectively, where the first one corresponds to the location of the mean of the 5–10% values of the cumulative frequency distribution and the second one corresponds to the mean of 90–95% values. The difference of these values gives an estimate of the EZT (Fig. 7). 30 s was the averaging time over which the EZT was calculated. The values of EZT for Case I are ranging from about 10 to 230 m (lower left panel) while the mean value of EZT derived by this technique is 75 m. Some higher values of EZT around 200 m might arise due to enhanced convective activity and associated entrainment of the FT air. This mean value of the EZT is approximately 20% smaller compared to the one obtained with the standard deviation method. High values of EZT (up to ~ 200 m) appear to be correlated with entrainment events of lower FT air.

Results obtained from the cumulative frequency distribution method for Case II show the estimated EZT values at each 30 s interval (upper right and lower right panel in Fig. 7). This technique yielded a mean EZT of 62 m while the maximum value of the EZT was 200 m. These types of high resolution measurements of the EZT can be used for experimental validation of the model formulated by Chemel and Staquet (2007) for a CBL.

In summary, a large difference was found between the values of EZT for these two methods. Both, Case I and Case II show that EZT obtained with the standard deviation method is higher than that with the cumulative frequency distribution method. One probable reason for the discrepancies can be due to the different intrinsic trends present in the time series of the CBL height. A more careful and an improved trend removal technique may help to reveal such trends in the time series. A detailed investigation of the differences found for EZT (17 m for Case I and 82 m for Case II) needs further

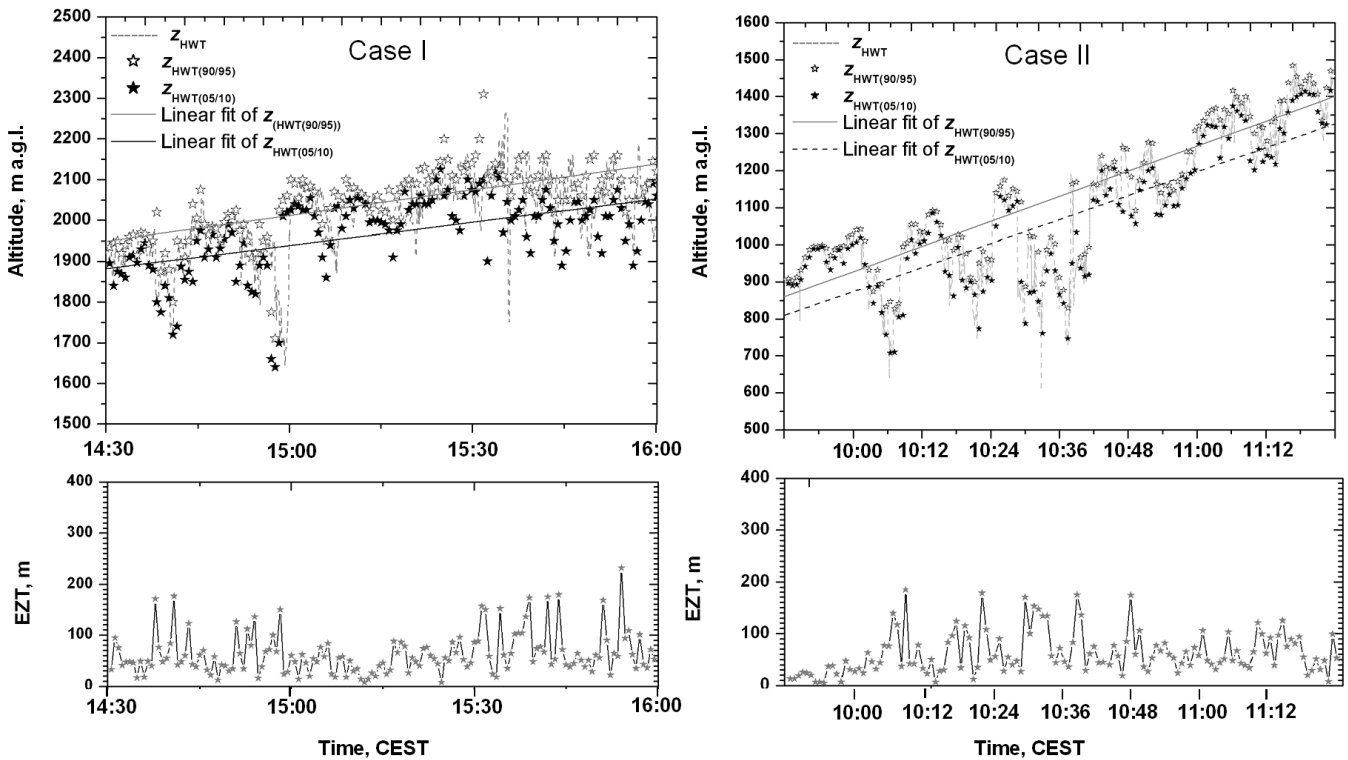


Fig. 7. EZT determined with cumulative frequency distribution of instantaneous CBL height (z_{HWT}) for Case I (left panel) and Case II (right panel) derived from 0.33 s resolution lidar data. Linear fits for both $z_{\text{HWT}(05/10)}$ (black-dashed line) and $z_{\text{HWT}(90/95)}$ (gray-dashed line) of the cumulative frequency distributions are also shown. The lower panels show the EZT for both cases.

research. Nevertheless, this regime (Case II) has rarely been considered in previous studies of the CBL entrainment zone characterization though being an important aspect with respect to near-surface air pollution.

5.4 Evolution of convective boundary layer height

Two different regimes of the CBL growth were clearly observed from the full-day time series of the lidar measurements, with respect to the estimated growth rate: one regime (from 09:55 to 11:15 CEST) with growth rate of 4–5 m/min and another (11:30 to 18:00 CEST) with comparatively slower rate with 0.5–2 m/min (Fig. 8). This figure shows the time series of CBL height growth rate in m/min (panel b) determined from the time series of the z_{HWT} estimated during 10:00–18:00 CEST (panel a). Evolution of the surface temperature (panel c) and rate of temperature change (with respect to time dT/dt , panel d) during the same period are also shown. Growth of the CBL height was highly correlated with temperature increase at the surface. Rapid growth in the morning was caused by surface heating and associated convective activities while the decrease of the growth rate and then the persistence of a constant slower growth were most probably due to interaction with the RL and resulting capping. The difference in CBL growth rates can be

explained by the surface heat flux behavior. However, details can depend on subsidence, atmospheric stability, etc., but a discussion of these effects on CBL growth rate is beyond the scope of the paper. The CBL height reached its maximum (2250 m) around 17:30 CEST. This suggests that the surface forcing was still present around this time. Sunset was at 21:30 CEST on this day.

It should be noted that the encroachment at the top of the CBL mentioned in Sect. 5 might be a result of the high correlation between the surface temperature and the CBL height measured during this time. Surface temperature observed during 10:00 and 11:30 CEST showed a sharp increase from 18.2 °C to 20.2 °C while the CBL height developed from 678–1545 m a.g.l. A correlation coefficient of 0.95 was found while comparing these two time series between 10:00 and 11:30 CEST. This is an indication to encroachment as the rapid growth of the CBL height is assumed to be highly dependent on the surface temperature while the RL atop remained more or less at the same altitude (around 1.7 km a.g.l.) with a slightly decreasing trend. Sorbjan (1996) showed in his work that early morning penetrative convection often evolves to an encroachment structure due to rapid growth.

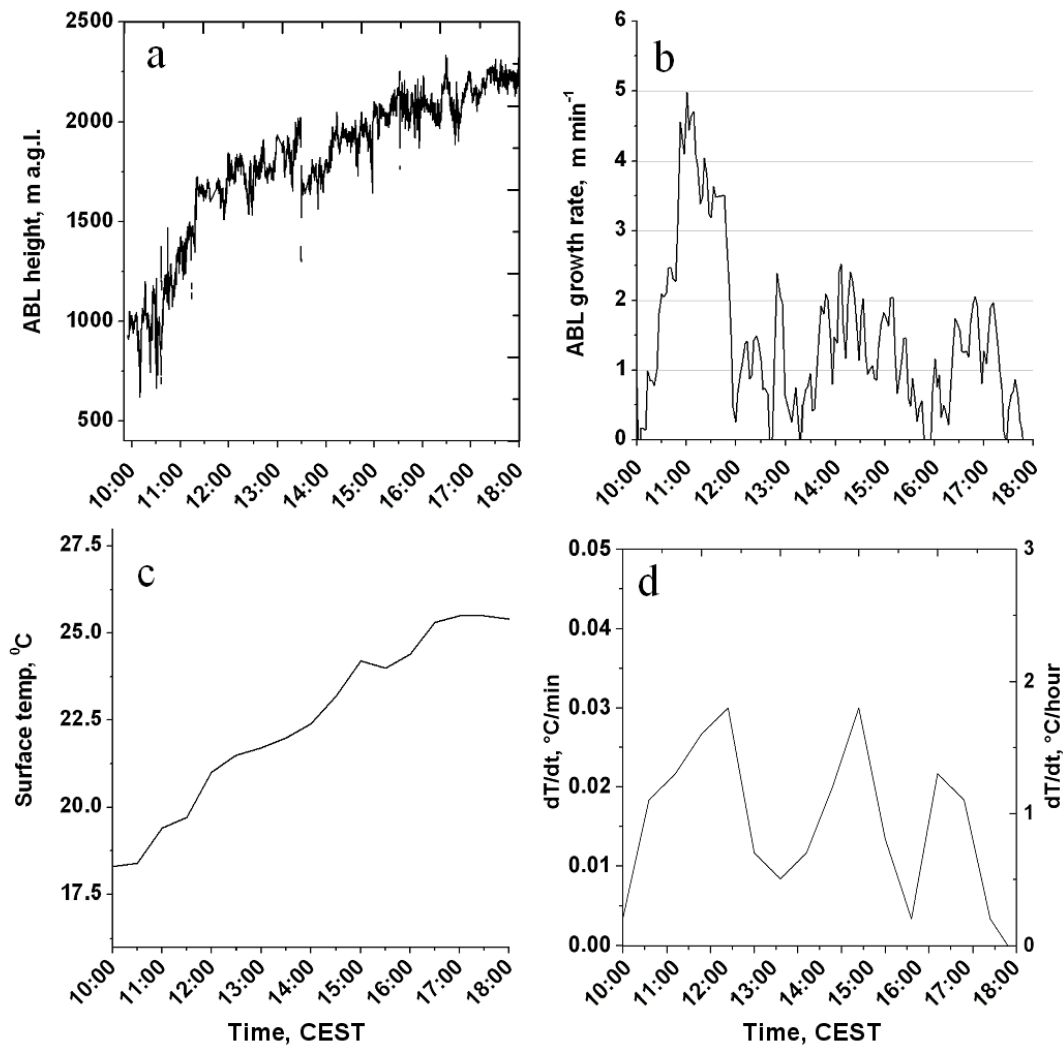


Fig. 8. The evolution of (a) the CBL height and (b) associated growth rate together with (c) surface temperature and (d) rate of temperature increase between 09:55 and 18:00 CEST on 26 June 2004. Two distinct regimes of CBL growth are found: one with 3–5 m/min and another with 0.5 to 2 m/min. The time series of CBL height and surface temperature between 10:00 and 11:30 CEST show a correlation coefficient of 0.95 indicating that surface heating is responsible for the CBL evolution in this period.

5.5 Vertical profiles of higher-order moments

So far, only the evolution of the CBL top has been discussed. To add further quantitative information, we determine the higher-order moments of particle backscatter coefficient fluctuations β'_{par} at different heights to study turbulence processes during both cases. Higher order statistics are derived up to an altitude of 2.7 km as it was found previously for these data sets that the CBL height was below 2.7 km a.g.l. We have shown the lower altitude for the vertical profiles of integral scale, variance, skewness, and kurtosis, to be 400 m a.g.l. Below this height, lidar data were affected by partial overlap of the transmitter-receiver geometry; one cannot use lidar data collected below these heights without further correction. It should be noted that in addition

to the normalized height z/z_i scale (z_i , mean CBL height) in the profiles of the higher order moments, we also kept the corresponding height in the figures.

5.5.1 Variance spectra

Figure 9 shows the variance spectra of relative particle backscatter coefficient for both observation periods at two different heights. Lidar data with time resolution of 10 s are used here since the errors due to instrument noise would have been unacceptably large at 0.33 s resolution for the purpose of higher-order moments estimation.

$\ln S_F(f)$ is plotted here against $\ln(f)$ where S_F is the spectral density and f is the frequency. The solid lines on the plots show the decrease of the spectra as expected according

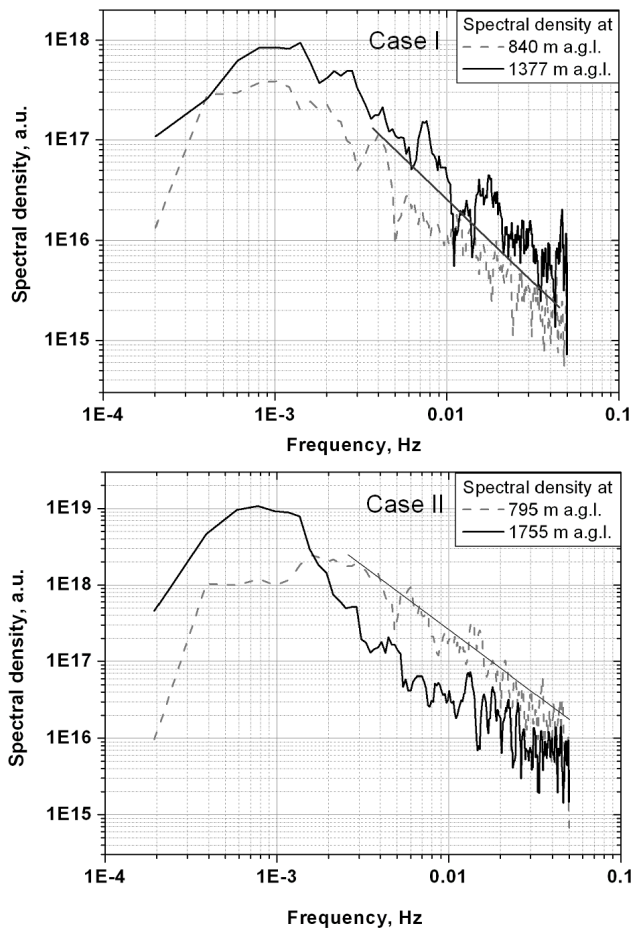


Fig. 9. Spectra of relative particle backscatter coefficient at two different heights for Case I (top) and Case II (bottom). The expected $-5/3$ -slope of the inertial subrange is shown in each panel.

to the $-5/3$ -power law describing the inertial subrange of the spectra (Kolmogorov, 1941). Obviously, the inertial subrange was reached in all cases. This confirms that the time resolution used here is high enough to resolve the energy containing eddies and part of the inertial subrange. Engelmann et al. (2008) showed similar characteristics in the variance spectra of β'_{par} for a case of well-mixed CBL confirming $f^{-5/3}$ roll-off in the spectra. The range resolution of the UHOH lidar (3 m) is higher than for their lidar (75 m) system. Variance spectra of relative particle backscatter coefficient fluctuations at two selected heights for Case II suggest that the inertial subrange was achieved here at the lower height while there is considerable deviation in the higher altitudes as can be seen from the spectra at 1755 m a.g.l.

5.5.2 Autocovariance

The second-order autocovariance function for each height level was calculated to determine the variance of the particle

backscatter and the corresponding noise variance. The autocovariance function calculated for 100 lags for four selected heights (1000, 1350, 1750, 2000 m for Case I and 600, 800, 1000, 1200 m for Case II) in the CBL are shown in Fig. 10. The increase of the total variance for zero lag (at 2000 m for Case I and 1200 m for Case II) was due to both the increase of the atmospheric variance and the noise variance. The atmospheric variance increased sharply because this altitude lies within the EZ.

5.5.3 Integral time scale

The integral time scale can be considered to be the temporal analogy to the integral length scale which is an average distance that energy and mass in the atmosphere can be transported down wind by large coherent eddies present. It is considered to be a useful parameter for numerical modeling of the turbulence and associated trace gas transport in the CBL. In turbulence measurements, a prerequisite for the resolution of the major part of turbulent fluctuations is that integral time scale $\gg dt$ where dt is the temporal resolution of the time series. If this condition is achieved, the major part of the horizontal variability of the turbulent eddies is sampled with acceptable resolution so that the inertial subrange in the spectrum and/or the dissipation range in the autocorrelation function becomes resolved. Simultaneously, the vertical resolution of the measurements must be smaller than the vertical coherence of the turbulent eddies. The high range resolution (3 m) in the UHOH lidar data helped to resolve vertical structures of turbulent fluctuations as will be shown here.

Following Lenschow et al. (2000), we have demonstrated the techniques for reasonable determination of the autocovariance functions extrapolated-to-zero-lag (described as $m_{11}(\rightarrow 0)$ in their study). In our work the extrapolation for this purpose is performed using the autocovariance function at lag one; we refer to this as 1st lag approach. Figure 11 shows the vertical distribution of the integral scale with and without noise correction for both cases. The profiles of integral scale and higher-order moments were normalized with the mean CBL height z_i of 2008 m and 1136 m for Case I and Case II, respectively. They were estimated by averaging the time series of z_{HWT} of those periods. These profiles clearly show that without noise correction the integral scale would be significantly underestimated. The standard error due to instrument noise is also shown.

The integral scale for Case I is mostly around 75 s inside the CBL but above $0.8 z_i$ this value decreases with height and attains 35 s near z_i . As shown in Fig. 11 for Case I, the integral scale values are lying between 40 and 90 s within the normalized height range of $0.2 z_i$ and $0.9 z_i$. An increase up to ~ 130 s was observed at $1.1 z_i$, which might be explained by strong entrainment occurring near the CBL top. The integral scale is always significantly larger than the time resolution of the lidar data. This means that roughly the first 5–9 lags of the autocovariance function fall within the inertial

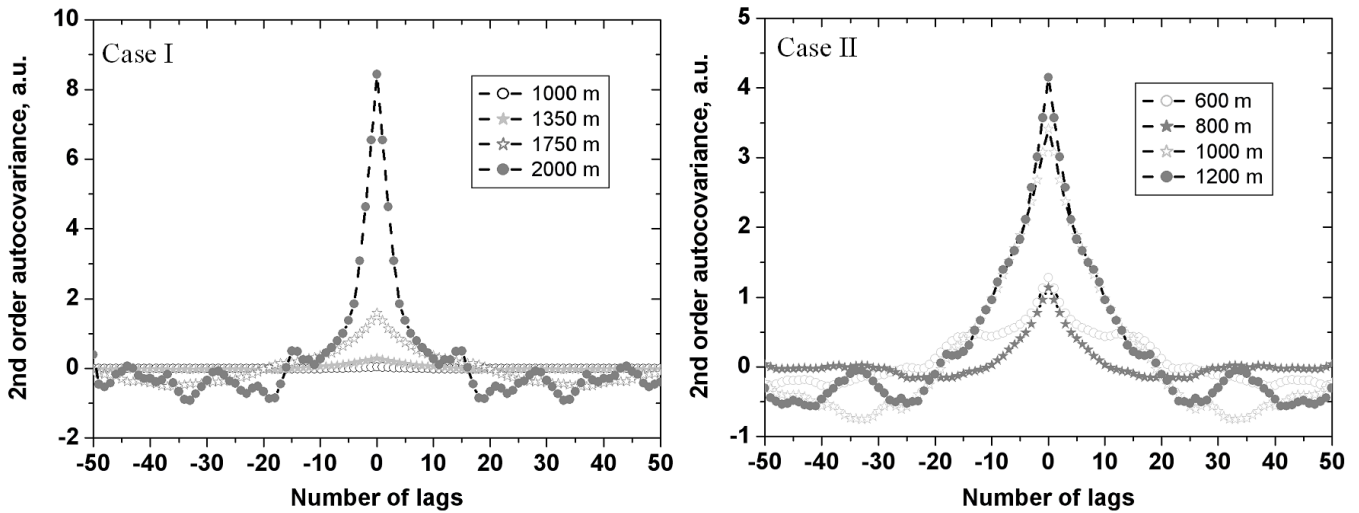


Fig. 10. Second-order autocovariance functions for four different heights for Case I (left) and Case II (right). The inertial range is resolved by only 5–7 data points. One lag corresponds to a shift of 10 s of the time series in the autocovariance function.

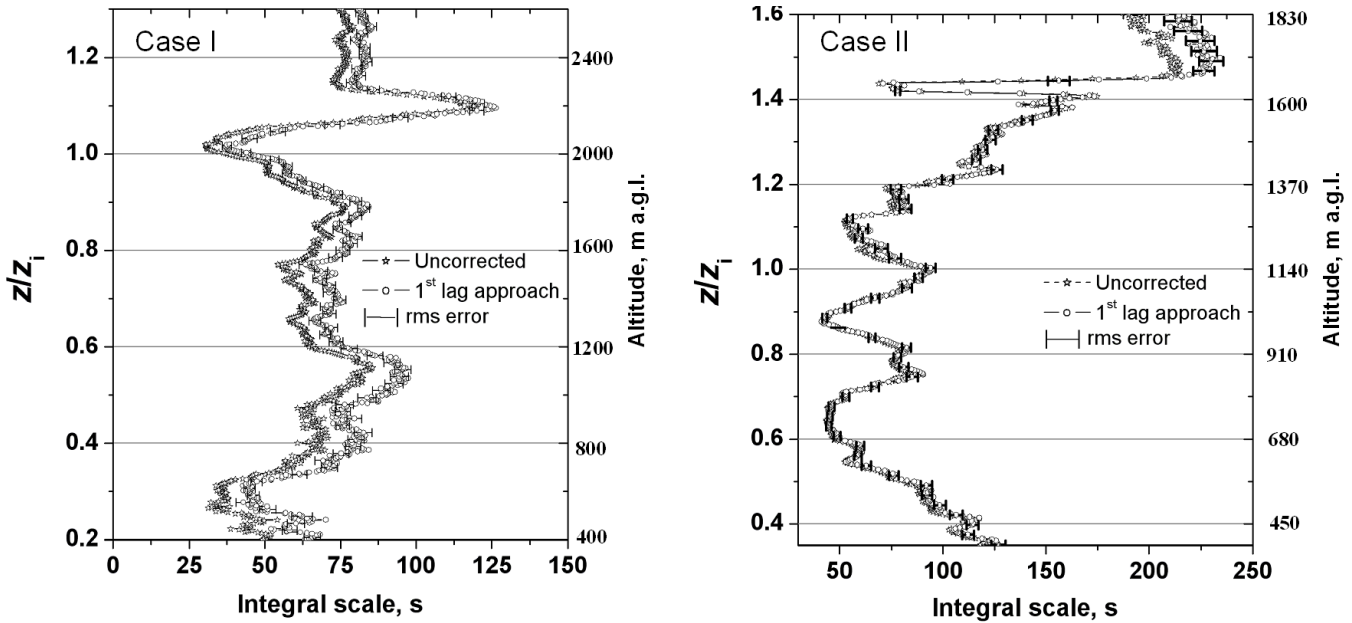


Fig. 11. The integral scale of particle backscatter coefficient fluctuations determined with and without noise correction for Case I (left) and Case II (right). The vertical coordinate is normalized with the mean boundary layer depth, i.e., the ratio of the height z and the mean CBL depth z_i of 2008 m and 1136 m for Case I and Case II, respectively. The error bars on the profile obtained with 1st lag approach denote the standard error due to instrument noise.

subrange. Therefore, the major part of turbulent fluctuations in the CBL can be resolved with the UHOH lidar data. This is the key feature of the high-time-resolution elastic lidar system of UHOH as it can be deployed to make turbulence statistics in the CBL. This is quite clear from the figure that a substantial decrease of integral scale is observed from $0.9 z_i$ to the top of the CBL. Couvreux et al. (2005) observed similar decrease of integral scale of moisture due to the presence

of dry tongue in the EZ while Kiemle et al. (1997) observed a slight decrease of the integral scale towards the top of the CBL.

Similar to Case I, the integral scale for β'_{par} during Case II was approximately 40–120 s inside the CBL (right panel, Fig. 11). Surprisingly, the vertical distributions of corrected and uncorrected integral scales are nearly the same except for altitudes above $\sim 1.5 z_i$. A prominent drop of the integral

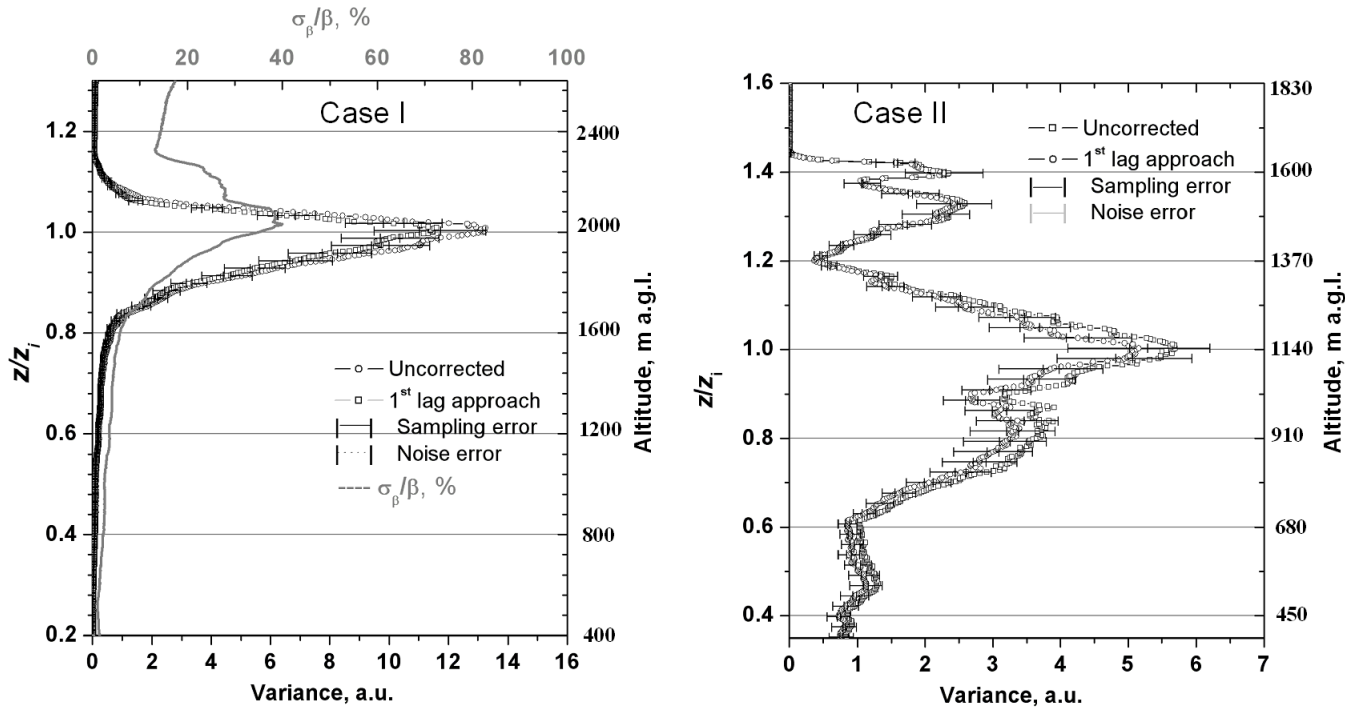


Fig. 12. Vertical distributions of the variance for Case I (left) and Case II (right) with noise correction (1st lag approach) and without any correction. The vertical coordinates are scaled as in Fig. 11. Statistical and sampling errors are plotted with the corrected profiles. A profile of σ_β/β is shown for comparison (solid gray line).

scale value at $1.4 z_i$, can be seen. Above $1.1 z_i$, an increasing trend was observed up to a high value of about 225 s from $1.5 z_i$ to $1.6 z_i$. However, it should be noted that the turbulence scales in the RL are likely much smaller than in the CBL. Consequently, 10 s time resolution used may not be appropriate to capture turbulence on the smaller scales. Therefore, it is more challenging to discuss in detail the integral scale in the region of the RL and an embedded thin AL with this technique. Furthermore, lidar measurements showed signatures of some organized wave activity associated with the RL. Consequently, the concept of random statistical atmospheric fluctuations may not be applicable here.

5.5.4 Variance

Vertical profiles of the variance with and without noise corrections for both cases are shown in Fig. 12. This figure shows that noise correction is only necessary between 0.8 and $1.1 z_i$. Variance profiles yielded the variability of the particle backscatter signal at different height above the lidar site for both periods. The profile for Case I shows that the variance of the aerosol distribution is approximately constant up to $0.8 z_i$ (~ 1600 m a.g.l.) since the vertical gradient of the aerosol concentration ($D(z)$ calculated for the entire period, not shown here) in this region are not large enough and nearly constant. The mean $D(z)$ profile confirmed that aerosol particles are uniformly distributed within this heights

implying that a well-mixed CBL regime prevailed. Above this height, variance increases reaching a well-defined maximum at 2022 m a.g.l. near the CBL top which is related to the large variation of aerosol concentration in the EZ due to rapid mixing of the air parcels between the CBL and the FT (Deardorff, 1972).

In a well-mixed CBL regime, very often sharp gradients in aerosol concentration exist through the EZ at the CBL top as cleaner from the FT is entrained and mixed into the aerosol-laden CBL. Since this variance profile (averaged over 1.5-h) can be considered as a space-averaged profile, the fluctuations of the inversion layer do not affect to the location of the maximum of the variance but make it more spread. This height can be considered as the mean CBL height over this time period indicating the location of most of the exchange processes between the CBL and the FT. These properties of the variance profile of β'_{par} are similar to the findings of Wulfmeyer (1999b) concerning the humidity variance, however, the shape near maximum is much sharper in the EZ in our case.

In contrast to the V profile of Case I, for Case II, there is a very broad peak between 700 m ($\sim 0.6 z_i$) and 1000 m ($0.9 z_i$), with a local maximum at a little above 910 m in addition to a sharp peak at the CBL top. There is a secondary broad peak between 1370 and 1650 m with a local maximum at a little below 1500 m. These correspond broadly with the CBL heights between 09:55–10:35 CEST and 11:00

to 11:15 CEST, with a period of more rapid growth between them (Fig. 5) and also likely due to the non-stationarities present in the CBL height evolution. However, the influence of the different aerosol layers cannot be ignored while explaining the vertical distribution of the variance in this case. Most probably, above $1.2 z_i$, high values of V corresponded to the RL and the AL at those heights. The rest of the large variance values were observed due to turbulent activities present in the CBL. Above the RL, the variance profile decreased and reached nearly a value of zero. Further investigation of these characteristics needs detailed information on flux Richardson number (Sorbján, 1990).

It should be noted that the dependence of the particle backscatter coefficient on RH is strongly related to the microphysical properties of the aerosol particles, particularly its hygroscopicity. Wulfmeyer and Feingold (2000) showed the relationship of the aerosol particle backscatter and humidity within the boundary layer based on state-of-the-art differential absorption lidar measurements of water vapor. Additionally, they compared their findings with an aerosol model based on the formulation introduced by Fitzgerald (1975) and Hänel (1976). Randriamiarisoa et al. (2006) showed that RH effect on aerosol microphysical properties is more complicated; for instance, hysteresis effects can cause backscatter lidar fluctuations. In Wulfmeyer and Feingold (2000), in the 70–80% RH region, the change of β_{par} was about 10%, in Gibert et al. (2007) it was between 10 and 20%, and in Randriamiarisoa et al. (2006) it was much larger in some cases, probably due to aerosol components particularly sensitive to RH. In our case, we are convinced that the site was mainly affected by urban aerosol particles so that based on the results of Wulfmeyer and Feingold (2000), the sensitivity in the 70–80% region should be in the order of 10%.

An important issue is the estimation of the variability of RH in the EZ. Unfortunately, only one radiosounding is available, which does not capture this variability. It showed the RH to be up to 70% within and above the CBL (Fig. 3). However, we are able to estimate this variability based on reasonable assumptions concerning boundary layer turbulence. Assuming reasonable summertime surface sensible and latent heat fluxes of 200 W m^{-2} , respectively, and a vertical convective velocity scale of $w_* \approx 1 \text{ m s}^{-1}$, we get a turbulent humidity scale of 0.08 g m^{-3} , and a turbulent temperature scale of $T_* \approx 0.16 \text{ K}$. Propagation of this variability in RH, e.g., using the Magnus equation, we estimate a variability of RH at the top of the CBL of about 5%. This translates in a variability of β_{par} of approximately 5% based on the results of Wulfmeyer and Feingold (2000). We have analyzed the profile of $\sigma_P/P \approx \sigma_\beta/\beta$, where σ_β is the square-root of variance and β is the mean profile of particle backscatter during the entire measurement period (Fig. 12). This profile shows the normalized variance (in %) of the particle backscatter fluctuation which considers only aerosol contribution to lidar backscatter signal. It shows that the variability of σ_β/β is about 40% in the EZ whereas we determined

a contribution of RH variability of just 5%. Consequently, we can state that the main variability of σ_β/β is determined by turbulence and not by RH fluctuations. Nevertheless, the analysis performed in this study illustrates the difficulties, but also the possibilities, of detailed analysis of aerosol lidar measurements for studying turbulence characteristics within a CBL.

5.5.5 Skewness

The turbulence structures throughout the entire CBL and above for both cases were further characterized by evaluating the vertical profiles of the skewness. Figure 13 shows the skewness profiles without and with noise correction using a three-point linear extrapolation to zero lag for both cases. Noise error and the sampling error are plotted as error bars on the corrected curve. Vertical structure of the skewness profile shows the presence of significant differences inside the CBL. The estimated noise error is small, but the sampling error is relatively high above the CBL top.

Skewness (third moment) is a measure of the lack of symmetry of a distribution. For Case I, within the lower half of CBL, we mostly observed skewness values close to zero (nearly Gaussian distribution) with exception of negative values in the regions near $0.4 z_i$. This indicates that the aerosol particles are evenly distributed (or well mixed) up to $0.5 z_i$. Within the upper half (i.e., between 0.5 and $0.9 z_i$) of the CBL, we observed negative skewness. Presence of these negative skewness values in these heights indicates very deep entrainment of clean FT air into the CBL and consequent mixing. The clean FT air gradually mixes with the aerosol particles inside the CBL and mixes out somewhere near the middle of the CBL and reflects highly negative perturbations. These observations are strikingly similar to the moisture skewness profile during the penetration of dry air pockets into the CBL as shown in Couvreux et al. (2005). Near the top of the CBL, a positive prominent peak is observed with S_k value of about 2. This is likely associated with the center of the aerosol plumes that are penetrating to this height.

For Case II, the skewness profile showed a high variability even inside the CBL with positive values. Predominant negative skewness values up to the height of $0.7 z_i$ were the result of rapid growth of the CBL height during Case II. Similar results were found by Mahr (1991), Couvreux et al. (2007), and Larson et al. (2001). For instance, Couvreux et al. (2007) clearly mentioned in their study: “The rapid CBL growth explains why greater negative skewness is observed during the growing phase...”. It should be noted that negative skewness is observed up to $\sim 800 \text{ m a.g.l.}$ This perhaps underlines the importance of entrainment processes down to very low altitudes during the rapid growth of CBL.

Above 800 m, positive skewness was found. It is interesting to note that the S_k profile increased with height in two different altitude regimes: one from $0.8 z_i$ and $1.1 z_i$ and the other from $1.2 z_i$ to the RL bottom at $1.45 z_i$. The first

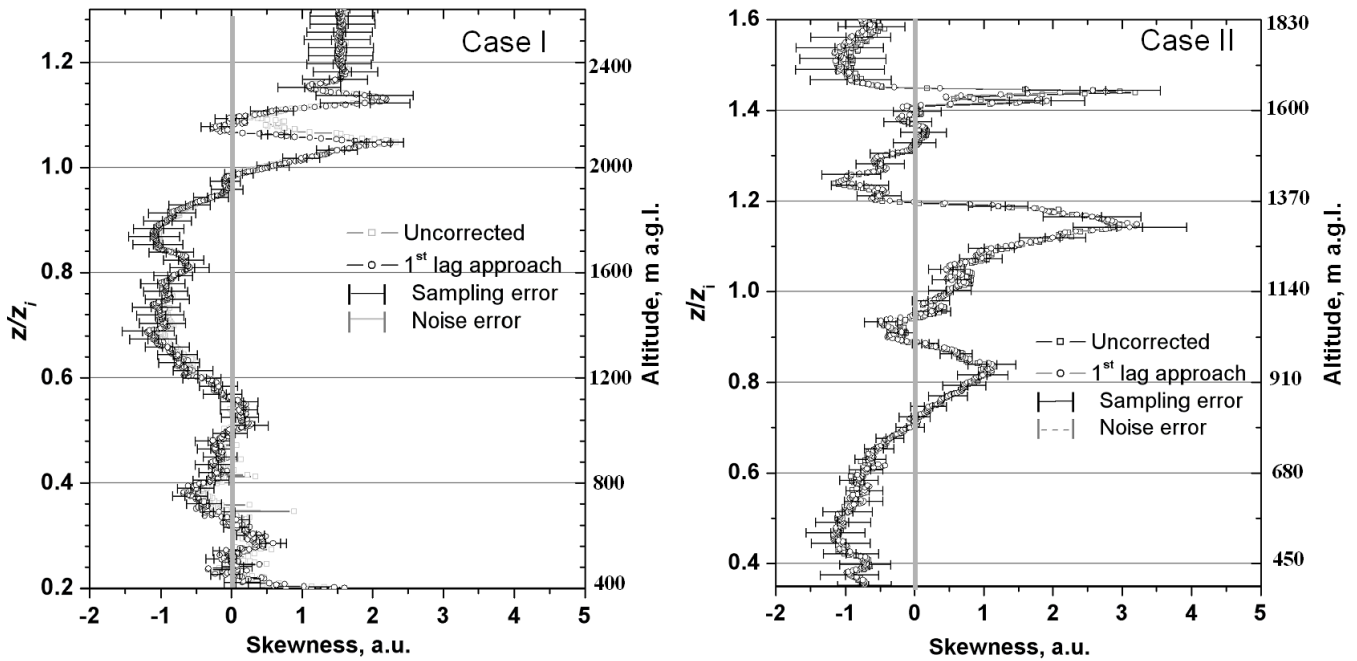


Fig. 13. Same as Fig. 11 but for skewness S_k for Case I (left) and Case II (right). For a Gaussian distribution, S_k is 0 (gray solid-lines).

is representative for convective activity, which organized as height increased but the second one exhibited several peaks, which were arising most probably due to the presence of different scales of mixing. Above an altitude of $1.5 z_i$, the S_k profile obtained a constant value close to -1 due to almost homogeneous aerosol distributions in the FT. It might be the case that the AL at 1.8 km has different turbulence characteristics than the RL; however, we can not accurately differentiate and quantify the differences between the AL and RL with the present data set. It should be noted that comparisons of these results with similarity relationships and scaling with standard turbulent scales in the CBL must be avoided.

5.5.6 Kurtosis

Figure 14 presents the kurtosis profile with and without noise correction for both cases. The sampling and noise errors are shown on the corrected kurtosis profile. First lag and linear fit approach provide here nearly identical results, so we kept the one corresponding to the first lag approach.

Kurtosis (fourth moment), a measure of the flatness of a distribution indicating whether the data distribution is narrow or flat relative to a normal distribution, is considered to be another important parameter in turbulence studies. In the present context, the value of kurtosis is expected to provide an indication of the degree of mixing at different heights.

Figure 14 shows a constant value of K around 3 corresponding to a nearly-Gaussian shape of the distribution of β'_{par} (for Case I) up to an altitude of $0.6 z_i$. However, between 0.6 and $0.9 z_i$ it shows a small increase of K between 4 and 5

which indicates that the distribution is more peaked here. K increases to 12 (four times larger than those of a pure Gaussian distribution) just above the top of the CBL which explains that the distribution has a more acute peak (around the mean) here than that within the CBL which might be arising due to the vigorous mixing at the regions of active entrainment dynamics. This agrees with the findings of Lenschow et al. (2000). A high value of K indicates that the most variability is due to the presence of infrequent extreme deviations in the time series of β'_{par} at those heights. On the other hand, a low value of K signifies a time series with most measurements clustered around the mean yielding a well-mixed CBL regime. For Case II, the kurtosis increased with height by a factor of ~ 2.5 in the region of CBL height.

5.6 Comparison of Case I and Case II

The key difference in the characteristics of the two cases is due to two main reasons. Firstly, a rapid growth of CBL height prevailed during Case II while for Case I, a very slow growth was found which could be considered as a quasi-stationary CBL. Secondly, unlike Case II, no strong RL or any detached multiple aerosol layers were observed during Case I. Similar behaviors were observed for both cases while demonstrating the CBL height estimation with LGM, IP method and the HWT-based analysis, i.e., the fundamental difference among the techniques providing $z_{\text{LGM}} > z_{\text{HWT}} > z_{\text{IP}}$.

Non-stationarity in the CBL height time series was explored using an FFT-based spectral analysis. Some studies

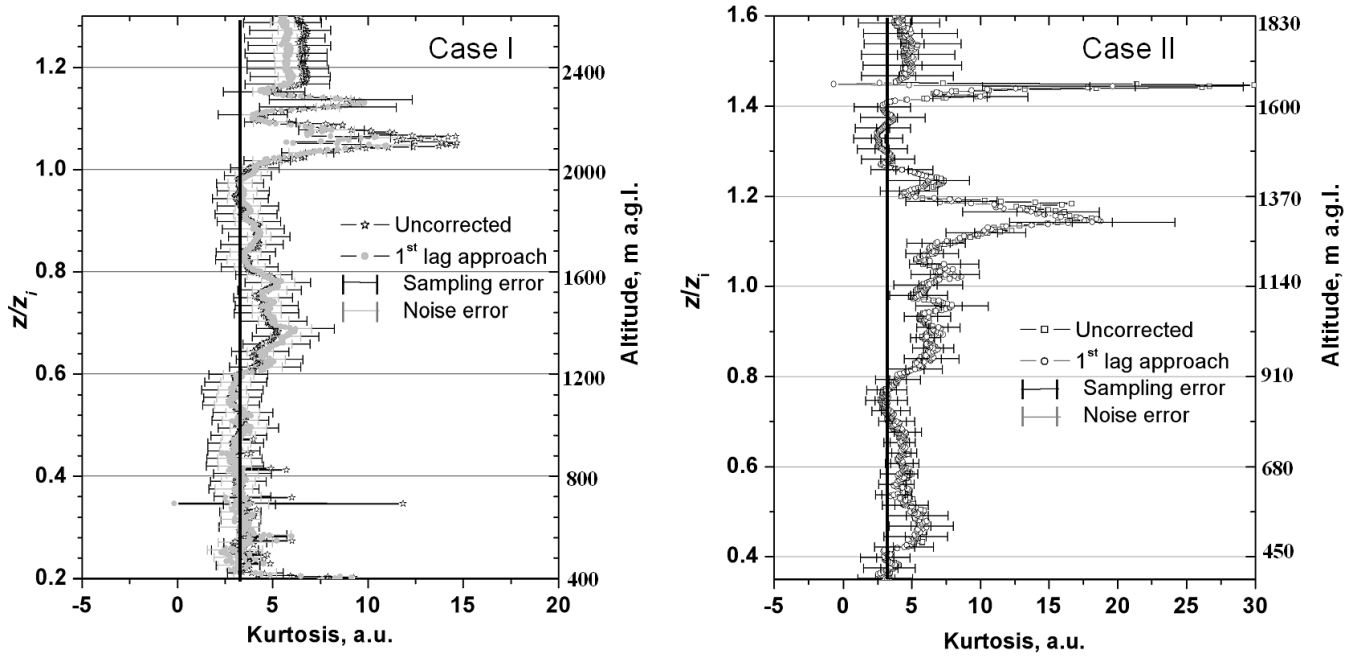


Fig. 14. Same as Fig. 11 but for kurtosis K for Case I (left) and Case II (right). A Gaussian distribution shows $K=3$ (vertical solid lines on both panels).

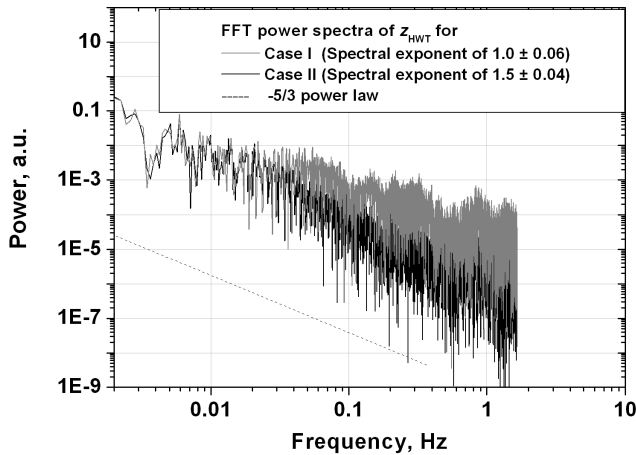


Fig. 15. FFT power spectra of the time series of z_{HWT} obtained for Case I (gray line) and Case II (black solid line). The $-5/3$ power law curve is shown for comparison. A spectral exponent value of 1.00 ± 0.06 and 1.50 ± 0.04 are found for Case I and Case II, respectively.

based on the time series analysis (e.g. Pelletier, 1997; Boers et al., 1995) have shown that the power-law dependence can be found from $S_F(f) \sim f^{-\gamma}$ where S_F is the power, f is the frequency and γ is the corresponding spectral exponent. The slope of $\ln[S_F(f)]$ versus $\ln[f]$ yields the value of γ . If $1 < \gamma < 3$ then, the signal is a non-stationary process with stationary increments. Davis et al. (1994) presented a detailed

discussion on the spectral properties and stationary issues for time series of geophysical datasets. Such FFT-based spectral analysis of the CBL height time series provided spectral exponent values of 1.00 ± 0.06 and 1.50 ± 0.04 for Case I and Case II, respectively (Fig. 15). For Case II, the spectral exponent value was lying in the region $1 < \gamma < 3$. This is a confirmation of the implicit non-stationarity present during Case II. For Case I, the spectral exponent value confirmed the quasi-stationary CBL regime. Additionally, there are some distortions in the low frequency tail of the spectrum of Case II. They are arising most probably due to the presence of a trend (an increasing one) in the time series producing non-stationarity in it. The temporal resolution of the analyzed time series is 0.33 s. Therefore, the Nyquist frequency ($f_{max}/2$) for the FFT spectra is 1.66 Hz. None of the slopes confirm the $-5/3$ -power law dependency. We conceive that the difference in the spectral exponent values is due to very different regimes of the convective activities present: the CBL time series, for Case I, this is entirely governed by the mixing in the EZ while for Case II, this is partially influenced by the entrainment in the RL atop.

Multifractal-based analyses can explore more details of non-stationarity regimes in CBL height time series as was shown in Pelletier (1997). The results can be applied for evaluating large eddy simulation (LES) results for investigating the structure of the inversion layers and associated entrainment in a CBL; Sullivan et al. (1998) showed promising results while performing similar spectral analysis on the CBL height time series. They found the spectral exponent

values to be dependent on the dynamic stability conditions in the CBL as well as to be sensitive to the grid resolution of the LES model used. These power law exponent values can be used operationally to separate stationary from non-stationary characteristics of CBL height on the basis of long term datasets. Furthermore, this information is beneficial to find some quantitative aspects of the time series. For instance, Perera et al. (1994) found the spectral exponent value to be 2 for intermittent wave breaking events in their mixing box experiments.

A detailed comparison among the vertical distribution of the higher-order moments profiles for both cases were already discussed in the previous section. Furthermore, it should be noted that the results obtained after the higher-order moments analysis are based on the assumption that hygroscopic growth of the aerosol particles can be neglected. It has been found that such assumptions are not considered to be fully true for the CBL regime during Case II both due to the heterogeneity in the distributions of the aerosol particles influenced by a rapid growth of CBL, and the presence of the RL and the AL above: certain sections of the profiles of higher-order moments thus include a mixture of data from above the CBL, within the active EZ, and within the body of the CBL. The relative fractions of each vary with altitude. Such a blending of data from different turbulent regimes affected the proposed interpretations of the profiles. However, it cannot be avoided that smearing takes place in regions with rapid CBL growth. Nevertheless, this kind of meteorological measurements are necessary for a description of the turbulence in the CBL regime even during its rapid growth as was shown in Couvreux et al. (2007) explaining the rapid growth to be the source of the negative water vapor skewness in the CBL.

6 Summary and outlook

Within this paper, the benefits of high-resolution measurements obtained with a vertically-pointing aerosol lidar for detailed CBL analyses are demonstrated. The data presented here, were collected over an urban region during an 8-h observing period in the daytime. The lidar system has spatial resolution of 3 m and a pulse repetition rate of 30 Hz, and therefore outperforms lidars used previously for such studies of the CBL and the entrainment zone, where high resolution measurements are highly beneficial.

The quasi-continuous vertically-pointing lidar measurements showed detailed insights into two different regimes of CBL on a certain day: a quasi-stationary well-mixed cloud free CBL (Case I) and a rapidly growing CBL in the morning in presence of a strong RL over the CBL top (Case II). Three different gradient-based approaches (LGM, IP, and HWT) are compared for precise determination of the instantaneous CBL height. Furthermore, EZT is determined. The HWT-based analysis is found to be the most robust technique. Ad-

ditionally, the HWT-based approach was successful in determining the CBL height also in complex situations like in Case II.

The evolution of the instantaneous CBL height through the course of the day is discussed. Two different growth rates are found: a high growth rate of up to 5 m/min in the morning and a relatively lower value of around 1 m/min in the afternoon. The instantaneous CBL heights varied between 0.6 and 2.3 km a.g.l. during the day. The mean EZT in the morning was lower (62 m) than in the afternoon (75 m). These values are obtained with the cumulative frequency distribution method. The spectral exponent value obtained in the energy spectrum for Case II, confirmed the non-stationary behavior. Its value of 1.50 ± 0.04 obtained for Case II is similar to the findings (1.60) of Boers et al. (1995) who investigated the ABL height in a trade-wind cumulus regime. These results can be applied for CBL modeling (Pelletier, 1997).

For the first time, aerosol lidar measurements were used for higher-order moments calculation of the aerosol backscatter field. This gave a comprehensive description of the atmospheric turbulence and aerosol inhomogeneities. This method can be applied for a well-mixed CBL regime if the fluctuations of aerosol microphysical properties can be neglected. It was demonstrated that the major part of the inertial subrange was detected and that the measured integral scales were significantly larger than the temporal resolution of the lidar data. Consequently, the major part of turbulent fluctuations was resolved. Power spectrum analysis of the aerosol backscatter fluctuations at various heights inside the CBL showed a roll-off according to $f^{-5/3}$ -power law which suggests that the inertial subrange was reached.

The vertical distribution of variance showed a well-defined structure with a maximum value at the top of the CBL without further peaks confirming an aerosol distribution in a regime of well-mixed CBL. However, the variance profile for the other case was found to consist of several peaks including the one at the mean CBL height. We found that the main contribution on the variance of particle backscatter coefficient is determined by turbulence not by RH. A contribution of RH variability of just 5% was obtained for Case I. A negatively-skewed structure of the aerosol distribution was found up to the top of the CBL and positive values of skewness were found in the EZ for the case of well-mixed CBL. Negative skewness values confirmed deep penetration of the clean FT air into the CBL for Case I. A high vertical variability with both positive and negative skewness inside the CBL was observed for the other case. The rapid growth of the CBL during Case II influenced substantially the skewness profile and yielded negative skewness in the lower half of the CBL. The integral scale profiles for both cases showed similar characteristics over the entire CBL height; e.g., a sharp decrease of the integral scale near the CBL top. These findings are qualitatively similar to the findings of Lenschow et al. (2000) who used in their study water vapor mixing ratio and vertical velocity while we use aerosol backscatter data.

It is important to mention here that in contrast to the quasi-continuous CBL, presence of different aerosol layers, a rapid growth of the CBL in the morning and a high non-stationarity during Case II made the distributions of the higher-order statistics in the CBL rather complicated so that the interpretation of the results was not straightforward. A major difficulty may arise if turbulent variables are compared with CBL similarity relationships and turbulent scales which are only defined in a quasi-stationary CBL; hence such comparison should be strictly avoided for Case II. Additionally, a detailed discussion on the turbulence profiles in the regions of RL and AL was not possible due to lack of resolution in our measurements and presence of waves. The analysis presented here can be improved if more information concerning the vertical profile of aerosol microphysical properties becomes available, e.g., by in-situ profiling or the application of multi-wavelength lidar systems. In future, we will combine aerosol backscatter measurements with water-vapor and temperature lidar measurements to detail more insights into the RH dependencies of particle backscatter coefficient. Climatology of these variables, e.g., collected with operational lidar system such as the SGP Raman lidar (Wulfmeyer et al., 2010) will be beneficial to characterize turbulence features in different regimes of CBL.

A deeper insight into the dependence of the variance of a scalar on scaling parameters in the CBL can be explored with the results obtained from LES models (Wyngaard and Brost, 1984; Moeng and Wyngaard, 1984) so that it becomes easier to demonstrate the characteristics which cause the sign and nature of the skewness profiles. These results can be a good basis for evaluating turbulent dispersion properties (e.g., non-Gaussian features) of aerosol plumes in various CBL regimes for instance through LES (Cai, 2000).

In future, this work will be extended to the study of the CBL turbulence with long-term measurements of atmospheric variables (e.g., water vapor mixing ratio, temperature, vertical velocity, aerosol measurements at different wavelengths) obtained with multi-instrument facilities during the international field campaign COPS (Convective and Orographically-induced Precipitation Study; Wulfmeyer et al., 2008).

Acknowledgements. We are grateful to our colleagues Max Schiller, Gerd Wagner, Anna Petrova-Mayor for their assistance and support during the measurement periods in Stuttgart downtown. We express our sincere thanks to Christoph Senff (NOAA, USA) for providing several IDL tools and fruitful discussions concerning data analysis. We also appreciate the effort of Olaf Tapfer for his help during the development of the lidar data acquisition software in Labview. The Nd:YAG laser was kindly provided by the Institute for Tropospheric Research, Leipzig, Germany. We also thank two anonymous referees for their valuable comments which led to substantial improvements to the manuscript.

Topical Editor F. D'Andrea thanks two anonymous referees for their help in evaluating this paper.

References

- Angevine, W. M., White, A. B., and Avery, S. K.: Boundary layer depth and entrainment zone characterization with a boundary layer wind profiler, *Bound.-Layer Meteorol.*, 68, 375–385, 1994.
- Baars, H., Ansmann, A., Engelmann, R., and Althausen, D.: Continuous monitoring of the boundary-layer top with lidar, *Atmos. Chem. Phys.*, 8, 7281–7296, 2008, <http://www.atmos-chem-phys.net/8/7281/2008/>.
- Behrendt, A., Wagner, G., Petrova, A., Schiler, M., Pal, S., Schaberl, T., and Wulfmeyer, V.: Modular lidar systems for high-resolution 4-dimensional measurements of water vapor, temperature, and aerosols, in: *Lidar Remote Sensing for Industry and Environment Monitoring V*, Proceedings of SPIE, edited by: Singh, U. N. and Kohei Mizutani, 5653, Honolulu, Hawaii, USA, 8–12 November 2004, 220–227, 2005.
- Behrendt, A.: Temperature Measurements with Lidar, in: *Lidar: Range-Resolved Optical Remote Sensing of the Atmosphere*, edited by: Weitkamp, C., Springer Series in Optical Sciences, vol. 102, ISBN: 0-387-40075-3, Springer, New York, 273–305, 2005.
- Beyrich, F. and Gryning, S.: Estimation of the entrainment zone depth in a shallow convective boundary layer from sodar data, *J. Appl. Meteorol.*, 37, 255–268, 1998.
- Boers, R., Eloranta, E. W., and Coulter, R. L.: Lidar observations of mixed layer dynamics: Tests of parameterized entrainment models of mixed layer growth rate, *J. Appl. Meteorol.*, 23, 247–266, 1984.
- Boers, R., Melfi, S. H., and Palm, S. P.: Fractal nature of the planetary boundary layer depth in the trade wind cumulus regime, *Geophys. Res. Lett.*, 22(13), 1705–1708, 1995.
- Boheren, C. and Huffman, D.: *Absorption and scattering of light by small particles*, Wiley, New York, 530, 1983.
- Brooks, I. M.: Finding boundary layer top: Application of a wavelet covariance transform to lidar backscatter profiles, *J. Atmos. Ocean. Technol.*, 20, 1092–1105, 2003.
- Cai, X.-M.: Dispersion of a passive plume in an idealized urban convective boundary layer: A large-eddy simulation, *Atmos. Environ.*, 34, 61–72, 2000.
- Chemel, C. and Staquet, C.: A formulation of convective entrainment in terms of mixing efficiency, *J. Fluid. Mech.*, 580, 169–178, 2007.
- Cohn, S. A. and Angevine, W. M.: Boundary layer height and entrainment zone thickness measured by lidars and wind-profiling radars, *J. Appl. Meteorol.*, 39, 1233–1247, 2000.
- Couvreur, F., Guichard, F., Redelsperger, J. L., Kiemle, C., Masson, V., Lafore, J. P., and Flamant, C.: Water-vapor variability within a convective boundary-layer assessed by large-eddy simulations and IHOP.2002 observations, *Q. J. Roy. Meteorol. Soc.*, 131, 2665–2693, 2005.
- Couvreur, F., Guichard, F., Masson, V., and Redelsperger, J.-L.: Negative water vapour skewness and dry tongues in the convective boundary layer: observations and large-eddy simulation budget analysis, *Bound.-Lay. Meteorol.*, 123, 269–294, 2007.
- Daubechies, I., Mallat, S., and Willsky, A.: Introduction to the special issue on wavelet transforms and multiresolution signal analysis, *IEEE Trans. Inf. Theory.*, 38(2), 528–531, 1992.
- Davis, A., Marshak, A., Wiscombe, W., and Cahalan, R.: Multifractional characterizations of nonstationarity and intermittency in geophysical fields: Observed, retrieved, or simulated, *J. Geophys.*

- Res., 99, 8055–8072, 1994.
- Davis, K. J., Lenschow, D. H., Oncley, S. P., Kiemle, C., Ehret, G., and Giez, A.: Role of entrainment in surface–atmosphere interactions over a boreal forest, *J. Geophys. Res.*, 102(29), 29218–29230, 1997.
- Davis, K. J., Gamage, N., Hagelberg, C. R., Kiemle, C., Lenschow, D. H., and Sullivan, P. P.: An objective method for deriving atmospheric structure from airborne lidar observations, *J. Atmos. Ocean. Technol.*, 17, 1455–1468, 2000.
- Deardorff, J. W., Willis, G. E., and Lilly, D. K.: Laboratory investigation of nonsteady penetrative convection, *J. Fluid Mech.*, 35, 7–31, 1969.
- Deardorff, J. W.: Numerical investigation of neutral and unstable planetary boundary layers, *J. Atmos. Sci.*, 29, 91–115, 1972.
- Degrazia, G. A., Anfossi, D., Carvalho, J. C., Mangia, C., Tirabassi, T., and Campos Velho, H. F.: Turbulence parameterization for PBL dispersion models in all stability conditions, *Atmos. Environ.*, 34, 3575–3583, 2000.
- Engelmann, R., Wandinger, U., Ansmann, A., Müller, D., Žeromskis, E., Althausen, D., and Wehner, B.: Lidar observations of the aerosol vertical flux in the planetary boundary layer, *J. Atmos. Ocean. Technol.*, 25(8), 1296–1306, 2008.
- Fitzgerald, J. W.: Approximation formulas for the equilibrium size of an aerosol particle as a function of its dry size and composition and ambient relative humidity, *J. Appl. Meteorol.*, 14, 1044–1049, 1975.
- Flamant, C., Pelon, J., Flamant, P. H., and Durand, P.: Lidar determination of the entrainment zone thickness at the top of the unstable marine boundary layer, *Bound.-Lay. Meteorol.*, 83, 247–284, 1997.
- Gamage, N. and Hagelberg, C.: Detection and analysis of micro fronts and associated coherent events using localized transforms, *J. Atmos. Sci.*, 50, 750–756, 1993.
- Gibert, F., Cuesta, J., Yano, J.-I., Arnault, N., and Flamant, P. H.: On the correlation between convective plume updrafts, lidar reflectivity and depolarization ratio, *Bound.-Lay. Meteorol.*, 125, 553–573, 2007.
- Hänel, G.: The properties of atmospheric aerosol particles as functions of relative humidity at thermodynamic equilibrium with the surrounding moist air, *Adv. Geophys.*, 19, 73–188, 1976.
- He, Q. S., Mao, J. T., Chen, J. Y., and Hu, Y. Y.: Observational and modeling studies of urban atmospheric boundary-layer height and its evolution mechanisms, *Atmos. Environ.*, 40, 1064–1077, 2006.
- Kiemle, C., Ehret, G., Giez, A., Davis, K. J., Lenschow, D. H., and Oncley, S. P.: Estimation of boundary layer humidity fluxes and statistics from airborne differential absorption lidar (DIAL), *J. Geophys. Res.*, 102(D24), 29189–29203, 1997.
- Kolmogorov, A. N.: The local structure of turbulence in incompressible viscous fluid for very large Reynolds numbers, *Doklady, ANSSSR* 30, 301–304, 1941.
- Lammert, A. and Bösenberg, J.: Determination of the convective boundary layer height with laser remote sensing, *Bound.-Lay. Meteorol.*, 119, 159–170, 2006.
- Larson, V. E., Wood, R., Field, P. R., Golaz, J. C., Vonder Haar, T. H., and Cotton, W. R.: Small-scale and mesoscale variability of scalars in cloudy boundary layers: one-dimensional probability density functions, *J. Atmos. Sci.*, 58, 1978–1994, 2001.
- Lenschow, D. H., Wulfmeyer, V., and Senff, C.: Measuring second- through fourth-order moments in noisy data, *J. Atmos. Ocean. Technol.*, 17, 1330–1347, 2000.
- Lothon, M., Lenschow, D. H., and Mayor, S. D.: Coherence and scale of vertical velocity in the convective boundary layer from a Doppler lidar, *Bound.-Lay. Meteorol.*, 121, 521–536, 2006.
- Martucci, G., Matthey, R., and Mitev, V.: Comparison between backscatter lidar and radiosonde measurements of the diurnal and nocturnal stratification in the lower troposphere, *J. Atmos. Ocean. Technol.*, 24, 1231–1244, 2007.
- Mahrt, L.: Boundary layer moisture regimes, *Q. J. Roy. Meteorol. Soc.*, 117, 151–176, 1991.
- Melfi, S. H., Spinhirne, J. D., Chou, S. H., and Palm, S. P.: Lidar observations of vertically organized convection in the planetary boundary layer over the ocean, *J. Climate Appl. Meteorol.*, 24, 806–821, 1985.
- Menut, L., Flamant, C., Pelon, J., and Flamant, P. H.: Urban boundary-layer height determination from lidar measurements over the Paris area, *Appl. Optics*, 38, 945–954, 1999.
- Moeng, C. H. and Wyngaard, J. C.: Statistics of conservative scalars in the convective boundary layer, *J. Atmos. Sci.*, 41, 3161–3169, 1984.
- Pal, S., Behrendt, A., Radlach, M., Schaberl, T., and Wulfmeyer, V.: Eye safe scanning aerosol lidar at 355 nm. Reviewed and Revised Papers of the 23rd International Laser Radar Conference (ILRC), Nara, Japan, 23–27 July 2006.
- Pal, S., Behrendt, A., Wulfmeyer, V., Valdebenito, Á. M., and Lamme, G.: A novel approach for the characterisation of transport and optical properties of aerosol particles emitted from an animal facility – Part I: Detection and analyses of aerosol plumes using a scanning eye-safe elastic UV lidar, *Atmos. Environ.*, submitted, 2010.
- Pelletier, J. D.: Kardar-Parisi-Zhang scaling of the height of the convective boundary layer and multifractal structure of cumulus cloud fields, *Phys. Rev. Lett.*, 78(13), 2672–2675, 1997.
- Perera, M. J. A. M., Fernando, J. S., and Boyer, D. L.: Turbulent mixing at an inversion layer, *J. Fluid Mech.*, 267, 275–298, 1994.
- Radlach, M., Behrendt, A., and Wulfmeyer, V.: Scanning rotational Raman lidar at 355 nm for the measurement of tropospheric temperature fields, *Atmos. Chem. Phys.*, 8, 159–169, 2008, <http://www.atmos-chem-phys.net/8/159/2008/>.
- Randriamiarisoa, H., Chazette, P., Couvert, P., Sanak, J., and Mégie, G.: Relative humidity impact on aerosol parameters in a Paris suburban area, *Atmos. Chem. Phys.*, 6, 1389–1407, 2006, <http://www.atmos-chem-phys.net/6/1389/2006/>.
- Russell, P. B., Uthe, E. E., Ludwig, F. L., and Shaw, N. A.: A comparison of atmospheric structure as observed with monostatic acoustic sounder and lidar techniques, *J. Geophys. Res.*, 79, 5555–5566, 1974.
- Schwemmer, G. K., Miller, D. O., Wilkerson, T. D., and Lee, S.: Lidar data products and applications enabled by conical scanning, edited by: Pappalardo, G. and Amodo, A., Reviewed and revised papers presented at 22nd International Laser Radar Conference, Matera, Italy, 12–16 July 2004, European Space Agency (SP-561), 17–20, 2004.
- Seibert, P., Beyrich, F., Gryning, S.-E., Joffre, S., Rasmussen, A., and Tercier, P.: Review and intercomparison of operational methods for the determination of mixing height, *Atmos. Environ.*, 34, 1001–1027, 2000.
- Senff, C. J., Bösenberg, J., and Peters, G.: Measurement of water

- vapor flux profiles in the convective boundary layer with lidar and Radar-RASS, *J. Atmos. Ocean. Technol.*, 11, 85–93, 1994.
- Senff, C. J., Bösenberg, J., Peters, G., and Schaberl, T.: Remote sensing of turbulent ozone fluxes and the ozone budget in the convective boundary layer with DIAL and radar-RASS: A case study, *Contrib. Atmos. Phys.*, 69, 161–176, 1996.
- Senff, C. J., Banta, R. M., Darby, L. S., Alvarez, R. J., Sandberg, S. P., Hardesty, R. M., and Angevine, W. M.: Ozone distribution and transport in the Houston area: Insights gained by airborne lidar, *Proceedings of AGU Fall Meeting*, San Francisco, California, USA, 6–10 December 2002, 173 p., 2002.
- Sicard, M., Perez, C., Rocadenbosch, F., Baldasano, J. M., and Garcia-Vizcaino, D.: Mixed-layer depth determination in the Barcelona coastal area from regular lidar measurements: Methods, results and limitations, *Bound.-Lay. Meteorol.*, 119, 135–157, 2006.
- Sorbjan, Z.: Similarity scales and universal profiles of statistical moments in the convective boundary layer, *J. Appl. Meteorol.*, 29, 762–775, 1990.
- Sorbjan, Z.: Effects caused by varying the strength of the capping inversion based on a large eddy simulation model of the shear-free convective boundary layer, *J. Atmos. Sci.*, 53, 101–112, 1996.
- Stull, R. B.: *An Introduction to Boundary Layer Meteorology*, Kluwer Acad. Publ., Dordrecht, 666, 1988.
- Stull, R. B. and Eloranta, E. W.: Boundary layer experiment, *B. Am. Meteorol. Soc.*, 65, 450–456, 1984.
- Sullivan, P. P., Moeng, C. H., Stevens, B., Lenschow, D. H., and Mayor, S. D.: Structure of the entrainment zone capping the convective atmospheric boundary layer, *J. Atmos. Sci.*, 55, 3042–3064, 1998.
- Taylor, G. I.: Diffusion by Continuous Movements, *Proc. London Math. Soc.*, 20, 196, 1921.
- Ulke, A. G.: New turbulent parameterization for a dispersion model in the atmospheric boundary layer, *Atmos. Environ.*, 34, 1029–1042, 2000.
- Wulfmeyer, V.: Investigation of turbulent processes in the lower troposphere with water-vapor DIAL and radar-RASS, *J. Atmos. Sci.*, 56, 1055–1076, 1999a.
- Wulfmeyer, V.: Investigations of humidity skewness and variance profiles in the convective boundary layer and comparison of the latter with large eddy simulation results, *J. Atmos. Sci.*, 56, 1077–1087, 1999b.
- Wulfmeyer, V. and Feingold, G.: On the relationship between relative humidity and particle backscattering coefficient in the marine boundary layer determined with differential absorption lidar, *J. Geophys. Res.*, 105(D4), 4729–4741, 2000.
- Wulfmeyer, V. and Janjić, T.: 24-h observations of the marine boundary layer using ship-borne NOAA high-resolution doppler lidar, *J. Appl. Meteorol.*, 44, 1723–1744, 2005.
- Wulfmeyer, V., Behrendt, A., Bauer, H.-S., Kottmeier, C., et al.: The Convective and Orographically-induced Precipitation Study: A Research and Development Project of the World Weather Research Program for improving quantitative precipitation forecasting in low-mountain regions, *B. Am. Meteorol. Soc.*, 89(10), 1477–1486, 2008.
- Wulfmeyer, V., Turner, D. D., Pal, S., and Wagner, E.: Can the water-vapor Raman lidar resolve profiles of turbulent variables in the convective boundary layer?, *Bound.-Lay. Meteorol.*, submitted, 2010.
- Wyngaard, J. C. and Brost, R. A.: Top-down and bottom-up diffusion of a scalar in the convective boundary layer, *J. Atmos. Sci.*, 41, 102–112, 1984.